Technical Report

TR-02-05

Inspection of copper canisters for spent nuclear fuel by means of ultrasound

Review of the research work performed in period 1994–2000

Tadeusz Stepinski, Ping Wu, Fredrik Lingvall
Uppsala University, Signals and Systems,
Department of Materials Science, Sweden

January 2002

Svensk Kärnbränslehantering AB
Swedish Nuclear Fuel
and Waste Management Co
Box 5864
SE-102 40 Stockholm Sweden
Tel 08-459 84 00
+46 8 459 84 00
Fax 08-661 57 19
+46 8 661 57 19

Inspection of copper canisters for spent nuclear fuel by means of ultrasound

Review of the research work performed in period 1994–2000

Tadeusz Stepinski, Ping Wu, Fredrik Lingvall
Uppsala University, Signals and Systems,
Department of Materials Science, Sweden

January 2002

This report concerns a study which was conducted for SKB. The conclusions and viewpoints presented in the report are those of the author(s) and do not necessarily coincide with those of the client.

1 Introduction

The research work in the project *Inspection of copper canisters for spent nuclear fuel by means of ultrasonic array system* that has been conducted at Signals and Systems, Uppsala University during the period of 1994-2000 is reviewed in this report. The review is based on the SKB reports and publications listed in the references [1-28] (Section 10). This report presents summaries of various tasks that were defined and performed at different periods of time according to the actual needs. The tasks that include both theoretical and experimental efforts may be classified into four main categories.

The first category,

(i) modeling of acoustic and elastic fields [1-4, 6-8, 11, 13, 15-18, 22, 25, 26]

is concerned with modeling of wave propagation in immersed solids (including acoustic and elastic waves). It was motivated by the lack of modeling tools required for the development of the experimental setups proposed for the inspection of copper canisters.

The second category, materials characterization, includes:

(ii) estimation of attenuation [7, 11, 17, 19, 22],

(iii) characterization of ultrasonic grain noise [7, 9, 11, 12], and

(iv) evaluation of electronic beam (EB) welds [17, 22, 23].

The evaluation of copper material and EB welds was the motivation behind this category.

The third category includes:

(v) imaging and signal processing [17, 20, 22, 24, 27, 28],

(vi) harmonic imaging [20, 21, 22, 24].

It was motivated by the need of improving defect imaging by the use of the advanced signal processing and ultrasonic imaging techniques.

The fourth category, that is concerned with the calibration and exploitation of the inspection system includes:

(vii) beam forming – focusing and steering [11];

(viii) detection and resolution limits of ultrasonic inspection [11];

(ix) transducer characterization [17, 22, 18, 19].

The motivation was ensuring that the inspection system would work properly and providing the correct information (signals) for the tasks in the first three categories. This report includes the task summaries in individual chapters organized in the order as they are listed above.

All the tasks were governed by the central goal of the project: ultrasonic inspection of copper canisters and EB welds. Here, the inspection includes defect detection and characterization, as well as the characterization of the parent copper material and the weld.

The research has been preformed mostly using the array ultrasonic inspection system ALLIN that has been used in our lab since 1995. For harmonic imaging we combined the ALLIN system with the MATEC TB-1000 tone burst card.

2 Modeling of acoustic and elastic fields

2.1 Introduction

Inspection of electronic beam (EB) welds in copper canisters using an ultrasonic array system motivated and initiated this task – modeling of acoustic and elastic fields. This modeling task has been carried out since 1994, and concerned with the theoretical aspects of the ultrasonic inspection. Theoretical knowledge about radiation and propagation of ultrasound is necessary to understand and provide a theoretical guidance to ultrasonic nondestructive evaluation (NDE). This task has shown its fundamental functionality in that the results created in this task have been employed in other tasks like estimation of attenuation (Chap. 3), characterization of ultrasonic grain noise (Chap. 4), harmonic imaging (Chap. 7), and transducer characterization (Chap. 10).

The ultrasonic array system, called ALLIN Ultrasonic Array System (simply called ALLIN system in sequel), that we have been using for the inspection was made by RD Tech, France (that used to be NDT System, France). The array is a linear array consisting of 64 strip-like transducers (elements) that are linearly aligned in azimuth (so that ultrasonic beams are electronically focused in azimuth) and all have cylindrically curved surface in elevation (so that beams are geometrically focused in elevation). The array was designed for use in pulse-echo mode and in immersion inspection. Therefore, the modeling of acoustic pulse fields in immersing fluids and elastic pulse fields in immersed solids from such a curved linear array was set as the main goal of the modeling task. Because we needed to use other types of transducers, e.g., spherically focused transducers, in other tasks like estimation of attenuation, characterization of ultrasonic grain noise, harmonic imaging, we have also modeled spherically focused transducers.

To achieve the main goal, we have extended three existing methods, listed below in order to adapt to our transducer geometry and application conditions.

(i) the angular spectrum approach (ASA), which is a frequency domain method
(ii) the Ocheltree and Frizzell's method (OFM), which is a frequency domain method, and
(iii) the spatial impulse response method (SIRM), which is a time domain method

The employment and extension of the above methods were motivated either due to the transducer geometry and application conditions or due to the computational efficiency. The ASA and OFM are frequency domain methods that are best suited for continuous waves, whereas the SIRM is a time domain method that is most appropriate for pulse (transient) waves. The three methods play different roles in the modeling.

The ASA is effective and efficient in calculating elastic fields in immersed solids. Thus, it is best suited for the immersion inspection of copper canisters. However, this approach could only be applied to planar transducers and arrays. Therefore, we extended the ASA to curved transducers [11, 13], and we have successfully modeled our curved linear array radiating acoustic fields in fluids and elastic fields in immersed copper materials.

The OFM of calculating acoustic fields was first established by Ocheltree and Frizzell for planar transducers and later applied by others to circular arrays. We first modified the OFM for cylindrically curved arrays radiating acoustic fields in fluids [7, 11]. Later we combined the OFM and the ASA and developed the indirect ASA that, like the extended ASA, could be used for the curved linear array radiating elastic fields in immersed solids [11, 13]. The indirect ASA was used as a comparative method when the extended ASA was developed for the curved linear array.

The ALLIN array works in pulse-echo mode, and its pulse excitation is, thus, required to model pulse ultrasonic (either acoustic or elastic) fields. To determine the pulse excitation we chose the SIRM that was the best candidate. However, the SIRM could only be applied to planar and spherically focused transducers before. Thus we extended the SIRM to cylindrically curved arrays, and obtained the pulse excitation to the ALLIN array [17,18]. Using the pulse excitation obtained from the SIRM and using the ASA, we have successfully modeled the elastic pulse transient fields in an immersed copper material from the ALLIN cylindrically curved array. For such a linear array we have also developed a tool for beam focusing and steering.

Besides, we also extended the ASA to axisymmetrically curved transducers, e.g., spherically circular transducers and spherically annular transducers, used for other tasks like estimation of attenuation, characterization of ultrasonic grain noise, harmonic imaging, and transducer characterization.

Based on the extended modeling methods, we have developed software tools for computing acoustic and elastic fields from transducers and arrays with a variety of shapes. It should be pointed out that as the results of the modeling task, the ASA, OFM and SIRM are further extendable to arbitrarily shaped transducers. In the following sections we will summarize these modeling methods and present a few selected results.

2.2 Theories for ultrasonic modeling

2.2.1 The (extended) angular spectrum approach (ASA)

The ASA is a powerful modeling tool that can be used to calculate acoustic fields in homogeneous and inhomogeneous (layered) media as well as elastic fields in immersed solids. The calculated fields

are continuos wave fields at a certain frequency ω. We first summarize the theory for the (extended) ASA to calculate acoustic fields from a transducer with an arbitrary shape. For the ALLIN array the shape is a cylinder. Then we present an application of the ASA in the case of an immersed solid plate, in which the reflected acoustic fields from the plate and the elastic waves in the plate are calculated. This application is representative, and shows a variety of fields that we can model: acoustic fields in a homogeneous fluid, reflected acoustic fields from a fluid/solid interface, elastic fields in an immersed solid, reflected elastic fields from a solid/fluid interface.

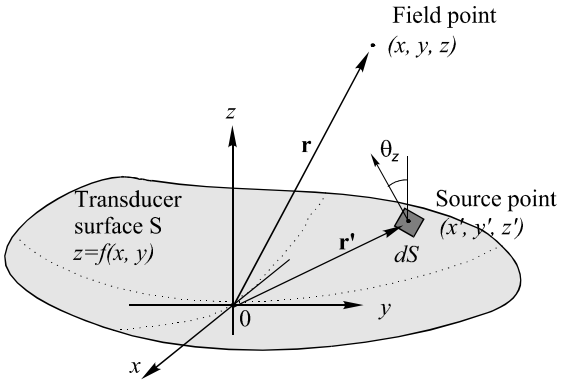

Fig. 2.1 The geometry and notations for the ASA to calculate an acoustic field from a transducer with an arbitrarily shaped surface S, $z = f(x, y)$.

A. Acoustic fields in a homogeneous fluid

In the ASA an acoustic field radiated from a transducer with an arbitrarily shaped surface S that is represented by $z = f(x, y)$ (Fig. 2.1) is calculated basically in the following two steps:

(i) Decompose the normal velocity distribution, $\tilde{v}(\mathbf{r};\omega)$, at frequency ω on the transducer surface S into a spectrum of plane waves with amplitude $V(k_x, k_y; z = z_1)$ in an initial plane $z = z_1$ ($z_1 \geq \max[f(x', y')]$) by using the double integral,

$$V(k_x, k_y; z = z_1) = \iint_{S_{xy}} \frac{\tilde{v}_n(x', y', f(x', y'))}{\cos\theta_z} \exp[-j(x'k_x + y'k_y)] \exp[j(z_1 - f(x', y'))k_z]\, dx'\, dy', \tag{2.1}$$

where S_{xy} is the area of the projection of the transducer surface S onto the x-y plane and $\cos\theta_z$ is the direction cosine of the normal with respect to the z-axis,

$$\cos\theta_z = \frac{1}{\sqrt{(f_x(x, y))^2 + (f_y(x, y))^2 + 1}}, \tag{2.2}$$

where $f_x(x, y)$ and $f_y(x, y)$ are the partial derivatives with respect to x and y, respectively, and the corresponding pressure plane wave at point (x, y, z) resulting from the normal velocity plane wave $V(k_x, k_y; z_1) \exp[j(xk_x + yk_y + (z - z_1)k_z)]$ is expressed as,

$$P(k_x, k_y; x, y, z) = k\rho_0 c V(k_x, k_y; z_1) \frac{\exp[j(xk_x + yk_y + (z - z_1)k_z)]}{k_z}, \quad (z \geq z_1), \tag{2.3}$$

where $k_x = kn_x$, $k_y = kn_y$, $k_z = \sqrt{k^2 - k_x^2 - k_y^2} = k\sqrt{1 - n_x^2 - n_y^2}$ are the spatial frequencies in the *x*-, *y*- and *z*-directions, respectively, and they define the propagation directions of the decomposed plane waves

(ii) Construct (or synthesize) the acoustic (pressure) field at field point (*x*, *y*, *z*) by superimposing all the decomposed plane waves travelling at (*x*, *y*, *z*) in the following way

$$\tilde{p}(x, y, z) = \frac{1}{(2\pi)^2} \int_{-\infty}^{\infty} \int_{-\infty}^{\infty} P(k_x, k_y; x, y, z) dk_x dk_y, \quad (z \geq z_1), \tag{2.4}$$

The alternative forms of Eqs. (2.1) and (2.4) in the polar coordinates are very useful, especially for transducers with axisymmetric geometries. A detailed study of axisymmetrically focused transducers, e.g., spherically focused transducers, has been presented in our recent SKB report [22].

B. Acoustic and elastic fields in the case of an immersed solid plate

Since the normal velocity on the transducer is decomposed into a set of plane waves (Eq. (2.1)), the properties of plane wave propagation can be used. Thus, the ASA is powerful in calculating ultrasonic fields in layered media with plane interfaces. A good application of the ASA is to ultrasonic immersion inspection of a copper canister block, in which the canister block (a plate with a front and a back surface and the thickness *D*) and the immersing fluid form a layered medium (Fig. 2.2). The ultrasonic fields in such a layered medium include acoustic fields reflected from the front and back surfaces of the plate and elastic fields in the plate. The acoustic and elastic fields can be constructed using the superposition of plane waves in the manner of Eq. (2.4). Therefore, an important issue for the ASA is to correctly work out the plane waves propagating in different layers.

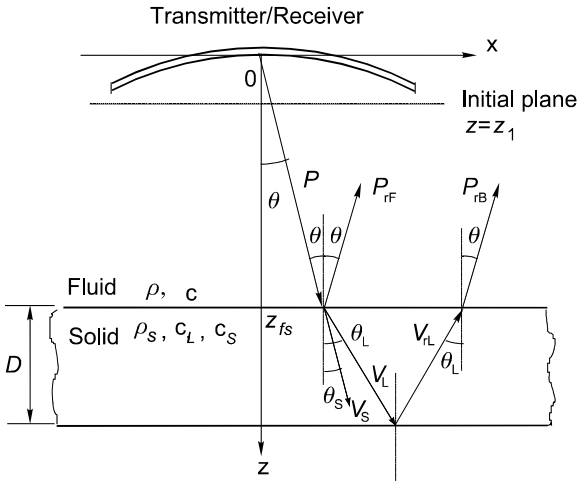

Fig. 2.2 The geometry and notations for the ASA to calculate acoustic fields reflected from and elastic fields in an immersed solid plate.

As shown in Fig. 2.2, one of the decomposed (pressure) plane waves, P, traveling in the fluid is incident on the front surface (a fluid/solid interface) at $z = z_{fs}$, and due to the mode conversion at the interface, there appears a reflected (pressure) plane wave P_{rF} in the fluid, a transmitted plane longitudinal wave (LW) $\mathbf{V}_L$ (particle velocity) and a transmitted plane shear wave (SW) $\mathbf{V}_S$ (particle velocity) in the immersed solid plate.

The LW and SW traveling in the plate encounter and reflect at the back surface (a solid/fluid interface). The reflected LW $\mathbf{V}_{rL}$, if we only consider the LW, propagates back in the plate, and then transmits into the fluid and turns to be the reflected (pressure) plane wave P_{rB} from the back surface at $z = z_{fs} + D$.

The incident plane wave $P(k_x, k_y; x, y, z)$ is directly formed from Eq. (2.3). The reflected and transmitted plane waves at the interfaces can be easily found from the Snell's law and the reflection and transmission coefficients at the front and back surfaces.

The reflected plane wave at the front is acoustic and given by

$$P_{rF}(k_x, k_y; x, y, z) = R_{fs}(k_x, k_y) P(k_x, k_y; x, y, z_{fs}) \exp\left[-j(z - z_{fs})k_z\right], \quad (z \le z_{fs}) \tag{2.5}$$

where $R_{fs}(k_x, k_y)$ is the reflection coefficient at the fluid/solid interface.

The transmitted LW at the front surface is elastic and given in terms of particle velocity by

$$\mathbf{V}_L(k_x, k_y; x, y, z) = \frac{\hat{\mathbf{L}} k_L T_{fs}(k_x, k_y) P(k_x, k_y; x, y, z_{fs}) \exp\left[j(z - z_{fs})k_{zL}\right]}{k\rho c},$$

$$(z_{fs} \le z \le z_{fs} + D), \tag{2.6}$$

where $T_{fs}(k_x, k_y)$ is the LW transmission coefficient at the fluid/solid interface.

The reflected LW at the back surface is elastic and written as

$$\mathbf{V}_{rL}(k_x, k_y; x, y, z) = \hat{\mathbf{L}}_r R_{sf}(k_x, k_y) V_L(k_x, k_y; x, y, z_{fs} + D) \exp\left[-j(z - z_{fs} - D)k_{zL}\right],$$

$$(z_{fs} \le z \le z_{fs} + D), \tag{2.7}$$

where $R_{sf}(k_x, k_y)$ is the LW reflection coefficient at the solid/fluid interface.

The (pressure) plane wave reflected from the back surface, which is due to the transmission of $\mathbf{V}_{rL}$, is acoustic and written as

$$P_{rB}(k_x, k_y; x, y, z) = \frac{k\rho c T_{sf}(k_x, k_y) V_{rL}(k_x, k_y; x, y, z_{fs}) \exp\left[-j(z - z_{fs})k_z)\right]}{k_L}, \quad (z \le z_{fs}). \tag{2.8}$$

Similarly the SW excited at the fluid/solid interface (front surface) and the SW reflected at the solid/ fluid interface (back surface) can be calculated.

The resulting acoustic fields, $\tilde{p}_{rF}$ and $\tilde{p}_{rB}$, reflected from the front and back surfaces of the plate, and the resulting, transmitted and reflected elastic LW fields, $\tilde{v}_L$ and $\tilde{v}_{rL}$, in the plate can be constructed all in the following manner

$$\tilde{g}(x, y, z) = \frac{1}{(2\pi)^2} \int_{-\infty}^{\infty} \int_{-\infty}^{\infty} G(k_x, k_y; x, y, z) dk_x dk_y, \quad (z \ge z_1). \tag{2.9}$$

The reflected acoustic fields from the front and back surfaces $\tilde{p}_{rF}$ and $\tilde{p}_{rB}$ have been used for diffraction correction for attenuation estimation (c.f., Chap. 3). The elastic LW velocity field, $\tilde{v}_L$, in the immersed solid has been calculated for a variety of arrays and transducers.

2.2.2 The Ocheltree and Frizzell's method (OFM)

The OFM is useful in the calculation of acoustic fields in homogeneous media. The transducer can be arbitrary shaped. The calculated fields are continuos wave fields at a certain frequency ω. The OFM is basically implemented in two main steps. The first step is dividing the transducer into such small rectangular subelements that the Fraunhofer (farfield) approximation can be applied; and the second step is superimposing the contributions of all the small elements to the resulting field.

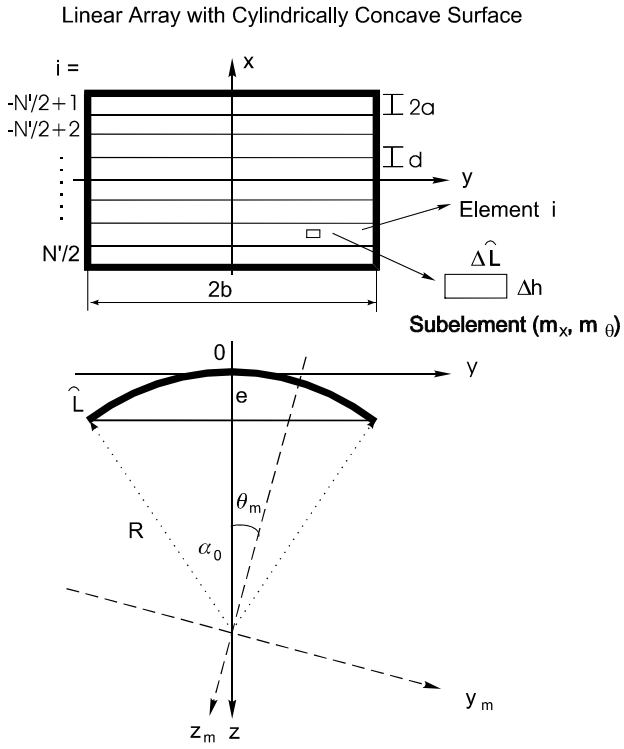

Fig. 2.3 The geometry and notations for the OFM to calculate an acoustic field from a linear array with a cylindrically concave surface.

Consider a linear array that has N' elements (N' is assumed to be even) and a cylindrically concave surface expressed by the following equation,

$$z = R - \sqrt{R^2 - y^2}\,,$$

$$\{x_i - a \le x \le x_i + a, \quad -b \le y \le b\} \qquad (2.10)$$

where R is the radius of the curvature, $2a$ and $2b$ define the width and length of each element, respectively, $x_i = (i - 1/2)d$ is the position of the center of the ith element on the x axis, i = -N'/2+1, ..., 0, 1, 2, ... N'/2, and z = e for $y = \pm b$. Each element is divided into such $M_x \times M_\theta$ small subelements with width $\Delta h = 2a/M_x$ and length $\Delta \hat{L} = \Delta\alpha R = 2\alpha_0 R/M_\theta$ (see Fig. 2.3) that the curvature of the subelements can be neglected, the subelements can be thought of as plane piston sources.

The pressure field from an array element whose center is located at the origin can, thus, be found,

$$\tilde{p}_{00}(x,y,z) = \frac{j\rho c \Delta A v_0}{\lambda} \sum_{m_\theta=1}^{M_\theta} \sum_{m_y=1}^{M_y} \mathrm{sinc}\left(\frac{k(x_m - x_{m_x})\Delta h}{2R_{sm}}\right) \mathrm{sinc}\left(\frac{k y_m \Delta \hat{L}}{2R_{sm}}\right), \qquad (2.11)$$

where

$$R_{sm} = \sqrt{(x_m - x_{m_x})^2 + y_m^2 + (z_m + R_0)^2} \tag{2.12}$$

$$\begin{bmatrix} x_m \\ y_m \\ z_m \end{bmatrix} = \begin{bmatrix} 1 & 0 & 0 \\ 0 & \cos\theta_{m_\theta} & \sin\theta_{m_\theta} \\ 0 & -\sin\theta_{m_\theta} & \cos\theta_{m_\theta} \end{bmatrix} \begin{bmatrix} x \\ y \\ z - R \end{bmatrix} \tag{2.13}$$

$$\theta_{m_\theta} = -\alpha_0 + \Delta\alpha(m_\theta - 1/2), \ (m_\theta = 1, \ ..., \ M_\theta). \tag{2.14}$$

The pressure field from the array can be obtained by summing up the fields from the N' elements,

$$\tilde{p}(x, y, z) = \sum_{i=-N'/2+1}^{N'/2} \tilde{p}_{00}(x + x_i, y, z). \tag{2.15}$$

2.2.3 The spatial impulse response method (SIRM)

The SIRM is useful in the calculation of acoustic fields in homogeneous media. The transducer can be arbitrary shaped. The calculated fields are pulse (transient) fields. The SIRM is basically implemented in three main steps: (i) dividing the transducer into such small rectangular subelements that the spatial impulse response of each rectangular subelement can be approximately expressed with the available analytical solution; (ii) superimposing the spatial impulse responses of all the small elements so as to create the resulting spatial impulse response; and (iii) convolving the resulting spatial impulse response with the pulse excitation to the transducer to construct the pressure field.

Consider a cylindrically curved, rectangular aperture that has dimension $2a \times 2b$ and radius of curvature R (see Fig. 2.4). The aperture is divided into such M sub-apertures of narrow strips with width ΔL and length $2a$ that each sub-aperture is approximately planar with dimension of $2\bar{a} \times 2\bar{b} = \Delta L \times 2a$, where

$$\Delta L = R\sin(\Delta\alpha/2), \ \Delta\alpha = 2\alpha_0/M, \text{ and } \alpha_0 = \arcsin(b/R). \tag{2.16}$$

The spatial impulse response (SIR) $h_{rect}(\mathbf{r}, t)$ of such a planar sub-aperture is available in analytical form (see [17]). From the superposition of the SIRs of all M sub-apertures, the SIR of the cylindrically curved, rectangular aperture can be written as,

$$h(\mathbf{r}, t) = \sum_{m=1}^{M} h_{rect}(\mathbf{r}_m, t), \quad (2.17)$$

where $\mathbf{r}_m = (x_m, y_m, z_m)$ is determined by the coordinates transform as follows,

$$\begin{bmatrix} x_m \\ y_m \\ z_m \end{bmatrix} = \begin{bmatrix} \cos\theta_m & 0 & \sin\theta_m \\ 0 & 1 & 0 \\ -\sin\theta_m & 0 & \cos\theta_m \end{bmatrix} \begin{bmatrix} x \\ y \\ z - R \end{bmatrix} \tag{2.18}$$

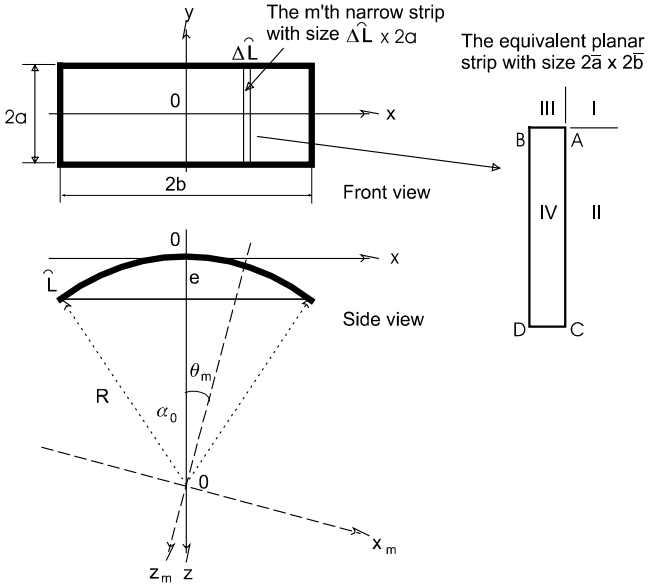

Fig. 2.4. Geometry of the rectangular aperture with cylindrically curved surface and the four regions (I, II, III, and IV) for the subaperture SIR.

$$\theta_m = -\alpha_0 + \Delta\alpha(m - 1/2)\,,\ (m = 1,\ \ldots,\ M\ ). \tag{2.19}$$

The pressure field at point **r** is given by the following relation,

$$p(\mathbf{r},t) = \rho \frac{\partial\left[v_n(t) * h(\mathbf{r},t)\right]}{\partial t}. \tag{2.20}$$

For a linear array consisting of the N elements as in Fig. 2.4, the SIR of the linear array without electronic focusing can be written as

$$h_{array}(\mathbf{r},t) = \sum_{i=1}^{N} h_0(x, y - y_i, z, t)\,, \tag{2.21}$$

where $h_0(\mathbf{r},t)$ is the SIR of the element centered at the origin and is calculated from Eq. (2.17), and $y_i = (i - N/2 - 1/2)d$ where $i = 1, 2, \ldots, N$

defines the center of the i'th element and d is the spacing of the adjacent elements. The pressure field of the array is given by

$$p_{array}(\mathbf{r},t) = \rho \frac{\partial\left[v_n(t) * h_{array}(\mathbf{r},t)\right]}{\partial t}. \tag{2.24}$$

2.3 Conclusions

To simulate acoustic transient fields in immersing fluids and elastic transient fields in immersed solids from the ALLIN array with cylindrically curved surface, we have extended three methods, the angular spectrum approach (ASA), the Ocheltree and the Frizzell's method (OFM), and the spatial impulse response method (SIRM).

The ASA and OFM work with continuous wave fields, whereas the SIRM is able to handle directly transient fields. In the SIRM the spatial impulse responses of a transducer are first calculated for given spatial positions, and then they are convolved with the normal pulse velocity on the transducer surface so as to result in the transient field.

The three methods have played different roles in our simulations. The ASA is an effective and efficient tool for calculating elastic fields in immersed solids while the SIRM is an important method for determining the pulse excitation of a transducer. Efficiency of the OFM when calculating continuous acoustic fields from the curved transducers is higher than that of the ASA and the SIRM.

The three considered methods have been applied to cylindrically curved ALLIN array, however, they can also be used to arbitrarily shaped transducers. All of them can be used to treat acoustic fields but only the ASA can be applied for calculating elastic fields in immersed solids.

We have developed the computer programs that compute the ultrasonic fields for the following transducer geometries:

(i) planar transducers with rectangular and circular geometries
(ii) planar arrays with rectangular and annular geometries
(iii) curved transducers with cylindrical and spherical geometries
(iv) curved arrays: linear arrays with cylindrical concave surface for geometric focusing, annular arrays with spherical focusing, and circular arrays.

It should be pointed out that the developed modeling methods can be further extended to arbitrarily shaped transducers. For linear arrays with planar or concave surfaces we have also developed a tool for designing beam focusing and steering laws.

3 Estimation of attenuation

3.1 Introduction

Ultrasonic attenuation in a metal material is related to the micro- and macro-structure and thus to the properties of the material. In other words, the attenuation in a material can be employed to evaluate the material's properties. Therefore, attenuation estimation has become one of the important issues in materials characterization. The main purpose of this task was to characterize the (copper) materials for copper canisters through quantitative estimation of attenuation, and the secondary purpose was to find attenuation for the need of the independent scattering model (ISM) used for characterizing ultrasonic grain noise (see Chap. 4).

In this task we have investigated two commonly-used methods, the spectral shift method (SSM) and the log-spectral difference method (LSDM), for attenuation estimation. Both methods could be applied to through-transmission mode and pulse-echo mode. We employed the methods in pulse-echo mode as we used the pulse-echoes from the front and back surfaces of plate samples in these methods. Since the SSM was easier to implement and showed to be more stable than the LSDM, we first exploited the SSM to find the attenuation for the need of the ISM [11]. However, the SSM only gives an appropriate estimation to such attenuation that is linear frequency dependent; whereas the LSDM may be used to estimate attenuation that is either linear or nonlinear dependent on frequency. The attenuation in a metal material, e.g., a copper canister, in fact, has shown to be nonlinear frequency dependent. In this case, the LSDM was a more appropriate estimation method so that we have used it together with diffraction correction.

The SSM and the LSDM are rigorously valid under the assumption of plane waves. In practice, however, the transducer used is usually finite sized and does not generate a plane wave field, instead a diffractive field, which is called diffraction (beam-spreading) effect. For a thin inspected sample, this diffraction effect is small so as to be neglected. When the inspected sample is thick, this effect may cause a significant error. Since the copper blocks we inspected were thick, we investigated the diffraction effect and its correction for the LSDM to achieve accurate estimation. It should be noted that the diffraction effect is transducer dependent. Thus, we conducted diffraction correction, respectively, for the ALLIN array, a spherically circular transducer, and a spherically annular transducer using the extended ASA that we developed for the array [17, 19] and the transducers [22]. The array is broadband and has a 3.1-MHz center frequency, and the two transducers, which actually

make up a concave annular array, are also broadband with center frequencies of 2.26, and 4.83 MHz, respectively. Thus, the array and the transducers cover different frequency bands, which form a broadened frequency range over which to estimate attenuation.

3.2 General consideration

Consider attenuation estimation in pulse-echo mode. Suppose the input pulse to an attenuating medium is $v_i(t)$ and has the amplitude spectrum $V_i(f)$ with central frequency f_i. After passing through the attenuating medium, the observed output pulse $v_o(t)$ is attenuated and its amplitude spectrum $V_o(f)$ with central frequency f_o can be written as,

$$V_o(f) = |H(f)| V_i(f), \tag{3.1}$$

where $|H(f)|$ is the transfer function, expressed as

$$|H(f)| = \exp[-\alpha(f) 2D], \tag{3.2}$$

where $\alpha(f)$ is the attenuation coefficient in the attenuating medium and is frequency dependent, and $2D$ is the two-way path length that the pulse $v_i(t)$ propagates. $v_i(t)$ and $v_o(t)$ can be either the pulse-echo signals from the front and back surfaces of a plate sample, or the backscattered signals from two different depths of a sample. The LSDM and the SSM are two methods that solve Eqs. (3.1) and (3.2) for $\alpha(f)$.

3.3 Log-spectral difference method (LSDM)

In the log-spectral difference method (LSDM) one takes the logarithms on both sides of Eq. (3.1) with Eq. (3.2) inserted into it. The attenuation coefficient is, thus, given by

$$\alpha(f) = \frac{\ln V_i(f) - \ln V_o(f)}{2D} \text{ (Np/cm)}. \tag{3.3}$$

Since Eq. (3.3) does not include the diffraction correction, its accuracy is good only when used for small values of D so that the beam does not spread enough to induce a significant error. $\alpha(f)$ in Eq. (3.3) is measured in nepers/cm (abbreviated Np/cm) when D is in cm. Another unit, dB/cm, is often used to measure $\alpha(f)$. For such a unit, $\alpha(f)$ is expressed, by use of the logarithm of base 10, as

$$\alpha(f) = \frac{20 \log V_i(f) - 20 \log V_o(f)}{2D} \text{ (dB/cm)}. \tag{3.4}$$

The conversion between the two coefficients is 1 Np = 8.686 dB.

When the thickness *D* of a specimen is not small, the diffraction (beam spreading) effect will result in a significant error. In this case, the diffraction effect correction becomes necessary.

3.4 Spectral shift method (SSM)

The spectral shift method is an alternative of the log-spectral difference method with the assumption that the input pulse $v_i(t)$ is Gaussian shaped and $\alpha(f)$ is a linear function of frequency. Assuming the central frequencies of the input and output signals, f_i and f_o, and the bandwidth of the input signal, *B*, the attenuation coefficient $\alpha(f)$ is given by

$$\alpha(f) = \frac{(2\pi)^2}{B^2}\frac{f_i - f_o}{2D} f \text{ , } \quad \text{(Np/cm),} \tag{3.5}$$

$$\alpha(f) = 8.686\frac{(2\pi)^2}{B^2}\frac{f_i - f_o}{2D} f \text{ , } \quad \text{(dB/cm).} \tag{3.6}$$

In practice, since $v_i(t)$ is Gaussian shaped, the Gaussian fitting is applied to both input and output amplitude spectra to determine f_i and f_o, and since $\alpha(f)$ is not a linear function of frequency, then the linear relation of $\alpha(f)$ with frequency is only valid in the vicinity of f_i. Our investigation has shown that that the SSM gave more stable estimations of attenuation than the LSDM.

Note that the spectral shift method always assumes $\alpha(f)$ to be a linear function of frequency and the input pulse $p_i(t)$ to be Gaussian shaped, and thus the output pulse $p_o(t)$ is Gaussian shaped, whereas the log-spectral difference method is not limited to $\alpha(f)$ to be a linear function of frequency.

3.5 Diffraction correction

When a specimen under inspection has a large thickness *D*, the diffraction (beam spreading) effect is necessary to correct.

Consider the attenuation estimation of a solid plate in the immersion measurement set-up shown in Fig. 3.1. Assuming that the incident pressure field radiated by the transducer is *p*(*t*), the reflected fields from the front and back surfaces are $p_{rF}(t)$ and $p_{rB}(t)$, whose spectra are $\tilde{p}_{rF}(\omega)$ and $\tilde{p}_{rB}(\omega)$, respectively, the longitudinal wave (LW) attenuation coefficient evaluated with diffraction correction is given by

$$\alpha_L(\omega) = \frac{1}{2D} \ln \left| \frac{\widetilde{p}_{rF}(\omega)/\widetilde{p}_{0rF}(\omega)}{\widetilde{p}_{rB}(\omega)/\widetilde{p}_{0rB}(\omega)} \right|, \tag{3.7}$$

where $\widetilde{p}_{0rq}(\omega)$ are the fields (usually calculated) with $\alpha_L = 0$.

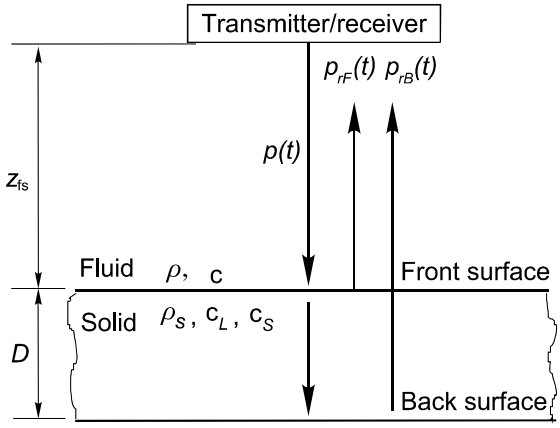

Fig. 3.1. Estimation of attenuation coefficient in a solid in the immersion measurement set-up.

If the attenuation in a fluid (usually water) is very small and neglected, we may have $\widetilde{p}_{rF}(\omega) = \widetilde{p}_{0rF}(\omega)$. Therefore, Eq. (3.7) becomes,

$$\alpha_L(\omega) = \frac{1}{2D} \ln \frac{\left|\widetilde{p}_{0rB}(\omega)\right|}{\left|\widetilde{p}_{rB}(\omega)\right|}, \tag{3.8}$$

α_L in Eqs. (3.7) or (3.8) is in Np/cm, and for dB/cm, use the conversion, 1 Np = 8.686 dB. In a real situation, $\widetilde{p}_{rq}(\omega)$ come from measurements, and $\widetilde{p}_{0rq}(\omega)$ from calculations (e.g. using the ASA).

3.6 Conclusions and discussions

To estimate attenuation in copper materials, two commonly used methods, the spectral shift method (SSM) and the log-spectral difference method (LSDM), and diffraction correction for immersion test have been investigated. The SSM has been used to estimate the attenuation coefficients in three copper specimens from High Profile Ultrasonics Ltd., England that had different structures [11]. The SSM gave the reasonable estimated results that showed that the copper block possessing coarser grains had a larger attenuation coefficient. The attenuation coefficients obtained from the SSM were subsequently used in the independent scattering model (ISM). The ISM yielded reasonable predictions to ultrasonic grain noise (see [11]).

The LSDM with diffraction correction has been applied to estimate attenuation in a copper block and a copper canister segment. The diffraction correction has been introduced, respectively, for the

ALLIN array, an spherically circular transducer, and a spherically annular transducer. The attenuation coefficients in the copper materials exhibited nonlinear frequency dependency. The investigation has shown that the copper canister segment has much smaller attenuation (about 0.19 dB/mm at 5 MHz) than the three copper blocks from High Profile Ultrasonics Ltd., England, whose attenuation coefficients were 1.84 – 2.31 dB/mm at 5 MHz.

The SSM is based on the assumptions that are hardly fulfilled in practice, namely that the input pulse into and the output pulse from the attenuating medium are Gaussian shaped, and that the attenuation is a linear function of frequency. Therefore, the attenuation estimation using SSM may have a fairly good accuracy only around the transducer's center frequency, and therefore the applying diffraction correction to the SSM might not be justified. The LSDM is much more accurate than the SSM and it can be applied for the estimation of attenuation being both linear and nonlinear function of frequency. The diffraction correction is always reasonable with the LSDM since it increases its accuracy compensating for the transducer beam-spread effects.

4 Characterization of ultrasonic grain noise

4.1 Introduction

Scattering and attenuation that occur when an ultrasound travels through a metal depend on the properties of materials. Thus, both scattering and attenuation have been employed to characterize the microstructure of metals. Although attenuation and scattering are closely related to each other, they can be used to deal with different problems.

The purpose of this task is to use the characteristics of ultrasonic grain noise for evaluating (characterizing) the properties of copper material. Two statistic models, the K-distribution model (KDM) and the independent scattering model (ISM) have been investigated.

In the KDM the grain noise is characterized with a parameter α that is related to the number of scatterers (grains). In general, for a fixed ultrasonic beam, the bigger the number of grains in the beam the larger the α.

In the ISM the normalized root-mean-square (rms) grain noise due to scattering from grains in a grainy material is estimated. The normalized rms is directly proportional to a specially defined parameter, called figure of merit (FOM) that is related to grain noise severity (the larger the FOM the coarser the grains, i.e., the severer the grain noise).

4.2 K-distribution model (KDM)

Ultrasonic grain noise results from the phase-sensitive detection of the scatters located in many randomly distributed sites within the resolution cell of a transducer. The process of interference can be described geometrically as a random walk. When an ultrasound pulse is transmitted into a random medium, the resultant complex amplitude of the backscattered ultrasound signal from the medium can be written as the sum of contributions from *N* independent scatters in the resolution cell

$$\mathbf{A}(\mathbf{r},t) = \sum_{n=1}^{N} \mathbf{a}_n(\mathbf{r},t) = \sum_{n=1}^{N} a_n(\mathbf{r},t) e^{j\phi_n(\mathbf{r},t)} = A(\mathbf{r},t) e^{j\phi(\mathbf{r},t)} \tag{4.1}$$

where $\mathbf{a}_n$ is the complex amplitude of the echo backscattered from the *n*th scatterer, a_n and ϕ_n are the amplitude and phase of $\mathbf{a}_n$, respectively, and *A* is the magnitude of **A**. It is assumed (i) that a_n and ϕ_n are random variables which are statistically independent from each other and from a_m and ϕ_m for

$m \neq n$, and (ii) that ϕ_n is uniformly distributed between 0 and 2π. N is also taken as a random variable and has a negative binomial distribution. Under these assumptions, the K-distribution is an appropriate model for this process.

The K-distribution is such that the probability density function (pdf) is expressed as

$$p(A) = \frac{2b}{\Gamma(\alpha)}\left(\frac{bA}{2}\right)^{\alpha} K_{\alpha-1}(bA), \qquad \alpha > 0 \tag{4.2}$$

where $\Gamma(\cdot)$ is the Gamma function, $K_{\beta}(\cdot)$ is the β th order of modified Bessel function of the second kind, and

$$\alpha = N(1+\upsilon), \quad (\upsilon > -1) \tag{4.3}$$

and

$$b = \sqrt{4\alpha / \langle a^2 \rangle}, \tag{4.4}$$

Here υ is the parameter related with the nonuniformity of the number density of scatterers (the number of scatterers in a unit volume) and the nonuniformity of the scattering cross section (that is related to the scatterer's dimension) and $\langle a \rangle$ is the scatterers' mean spacing. The K-distribution has two parameters, α and b (that is determined by both α and $\langle a^2 \rangle$). α is related to the number density of scatterers and can be used to characterize ultrasonic grain noise.

To find α, we use the normalized 1*st*, 4*th* and 6*th* order central moments given, respectively, by

$$r_1 = \frac{\langle A \rangle}{\langle A^2 \rangle^{1/2}} = \frac{\sqrt{\pi}}{2}\frac{\Gamma(1/2+\alpha)}{\sqrt{\alpha}\Gamma(\alpha)} \tag{4.5}$$

$$r_4 = \frac{\langle A^4 \rangle}{\langle A^2 \rangle^2} = 2\left(1+\frac{1}{\alpha}\right) \tag{4.6}$$

and

$$r_6 = \frac{\langle A^6 \rangle}{\langle A^2 \rangle^3} = 6\left(1+\frac{1}{\alpha}\right)\left(1+\frac{2}{\alpha}\right), \tag{4.7}$$

where the *m*th order central moments of magnitude A for the K-distribution are given by

$$\langle A^m \rangle = \left(\frac{\langle a^2 \rangle}{\alpha}\right)^{m/2} \frac{\Gamma(m/2+\alpha)\Gamma(m/2+1)}{\Gamma(\alpha)}. \tag{4.8}$$

From Eq. (4.5), we can find a solution for α, which is denoted by α_1, by numerical calculation of Eq. (4.5). From Eqs. (4.6) and (4.7), we can easily find anther two solutions for α, which are written, respectively, as

$$\alpha_4 = \frac{2}{r_4 - 2} \tag{4.9}$$

and

$$\alpha_6 = \frac{9 + \sqrt{9 + 12 r_6}}{r_6 - 6}. \tag{4.10}$$

Generally, in the absence of single strong scatterers in a region of interest (ROI), the pdf's of the K-distribution resulting from the estimated α were in excellent agreement with the pdf obtained from the measured data. In this case, the bigger the number of grains in the insonifying ultrasonic beam the larger the α. In the presence of defect(s), we may have $\alpha_1 > \alpha_4 > \alpha_6$, which can be used as a feature for defect detection [7, 9]. The pdf's of the K-distribution deviated the pdf's obtained from the measured data.

4.3 Independent scattering model (ISM)

The independent scattering approximation (properly defined) can be interpreted as the first term in a systematic expansion for the backscatter signal. The geometry for the ISM is shown in Fig. 4.1.

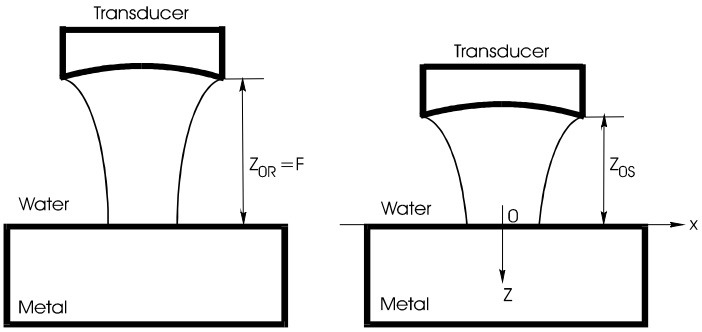

Fig. 4.1. Geometries for (a) reference signal acquisition and (b) noise measurement.

The water paths Z_{0R} for the reference signal and Z_{0S} for the noise measurement are measured outward from the transducer face along the central ray direction. The coordinates for the points in the metal are measured from the intersection of the central ray and the water/solid interface (Fig. 4.1).

Assuming that the total noise signal $S(t, x, y, z)$ is an incoherent superposition of noise signals backscattered by the individual grains of the metal (i.e., only single-scattering events is considered explicitly), and that the attenuation of the beam with depth will be treated through an effective attenuation constant, the ISM is given by

$$\frac{\sqrt{\left\langle \widetilde{S}^2(\omega) \right\rangle}}{\widetilde{V}_{ref}(\omega)} = n^{1/2} \left| \overline{A}(\omega) \right| \frac{2T_{01}^2 \rho_1 v_1 \exp[-2\alpha_0 (z_{0S} - z_{0R})]}{R_{00} a^2 \rho_0 v_0 |D(\omega)| k_1} \left[\int_0^\infty P \exp(-4\alpha_1 z) dz \int_{-\infty}^{\infty} \int_{-\infty}^{\infty} |C(\omega, x, y, z)|^4 \, dx dy \right]^{1/2} \tag{4.11}$$

where

c – longitudinal wave velocity,

$k = \omega / c$ – wave number,

ρ – density,

α – attenuation coefficient, and

a – transducer radius.

The subscripts 0 and 1 refer to water and metal; R_{00} and T_{01} are the reflection and transmission coefficients for plane wave velocity fields propagating in the central-ray direction; $C(\omega,x,y,z)$ is a measure of ultrasonic field strength in the metal; and n is the volume density of grains; $D(\omega)$ accounts for the effects of diffraction losses in the reference signal; and $\overline{A}(\omega)$ is an averaged grain backscatter amplitude at frequency ω.

The ISM in Eq. (4.11) predicts the normalized root-mean-squared (rms) grain noise, $N(t)$,

$$N(t)=\frac{n(t)}{E_{\max}}, \tag{4.12}$$

which is determined from the measurements, and in which $E_{\max}$ is one half of the peak-to-peak voltage of the reference signal, and

$$n(t)=\left[\frac{1}{M}\sum_{m=1}^{M}\left(V_m(t)-b(t)\right)^2\right]^{1/2} \tag{4.13}$$

is the rms deviation of grain noise from the background $b(t)$ given by

$$b(t)=\frac{1}{M}\sum_{m=1}^{M}V_m(t)\,. \tag{4.14}$$

where $V_m(t)$ is the measured signal voltage at time t for transducer position m in the M transducer positions of acquiring data. Note that the grain noise rms, $N(t)$, which is shown as a function of time may be regarded as a function of depth within the specimen. In the ISM $n^{1/2}\left|\overline{A}(\omega)\right|$ is an important parameter that is referred to as figure of merit (FOM). From Eq. (4.11) it follows that the normalized rms grain noise is directly proportional to the FOM related to the grain noise severity (the larger the FOM the coarser the grains).

4.4 Conclusions

Two statistical methods, the KDM and the ISM, have been investigated and applied to characterizing ultrasonic grain noise in copper materials with different grades (grain sizes).

In the KDM the parameter α is related to the number density of scatterers. The results have shown that the coarser the grains, i.e., the less the number density of grain, the smaller the α.

In the ISM the figure of merit (FOM) is related to grain noise severity (coarseness). The use of the ISM for grain noise characterization has revealed that the coarser the grains are (i.e., the severer the grain noise) the larger the FOM becomes.

From this and the preceding chapter, it can be concluded that material properties can be indirectly characterized by grain noise characterization or by attenuation estimation. There are a number of methods that can be used for grain noise characterization and attenuation estimation.

5 Evaluation of EB welds

5.1 Introduction

The aim of this task is to evaluate electron beam (EB) welds with respect to their macro- and microstructure. This is of great help for developing ultrasonic methods capable of detecting flaws in the weld. The EB welds have been evaluated by means of ultrasonic imaging, statistical analysis of scattering properties, and estimation of their velocity and attenuation.

Ultrasonic imaging of an EB weld has been performed as A-, B-, and C-scans. A C-scan provides a top (or longitudinal) view of an EB weld in a copper canister, whereas a B-scan shows a cross-sectional (transverse) view of the weld. An A-scan may be used for signal analyses and processing and for more precise parameter estimation, e.g., estimation of the time of flight. The three types of scans are complementary.

An EB weld has the form of a layered structure consisting of a host material zone (HMZ), a heat-affected zone (HAZ), and a fusion zone (FZ). Because of this layered structure, we proposed a method of choosing best time windows for all individual layers based on the statistical property of ultrasonic scattering in the weld. Thus, more detailed information on each individual layer of the weld can be obtained. The grain size in each layer differs very much (usually grains are fine in the HMZ, get bigger in the HAZ, and become coarse in the FZ). Statistical analysis of ultrasonic properties of scattering from a weld facilitates characterizing the layered structure.

Because of the difference of grain sizes in the HMZ, HAZ, and FZ, the contrast of each zone in the image is different. To obtain a satisfactory contrast in the image for both the HAZ and FZ of an EB weld, we proposed to use an annular array consisting of two elements with different center frequencies. The element with a frequency of 4.5 MHz gives a satisfactory contrast to the HAZ images, and the other element having a frequency of 2.3 MHz gives the FZ a satisfactory contrast so that the HAZ and FZ could be clearly distinguished and the weld parameters estimated, e.g., the thickness of the HAZ and HZ, and the grain sizes in different zones.

Ultrasonic properties of EB welds and host material, such as, ultrasonic velocity, attenuation and reflectivity have been further investigated in order to gain a deeper insight into the mechanism of formation of ultrasonic signals from the welds and defects.

5.2 Ultrasonic imaging of EB welds using the ALLIN array

EB welding is a fusion welding process in which heating results from the impingement of a beam of high-speed electrons on the metal to be welded. In general, a single-run fusion weld consists of a fusion zone (FZ) and a heat-affected zone (HAZ) that are embedded in the host material zone (HMZ). Inspection of EB welds has been made using the ALLIN ultrasonic array system in our previous work.

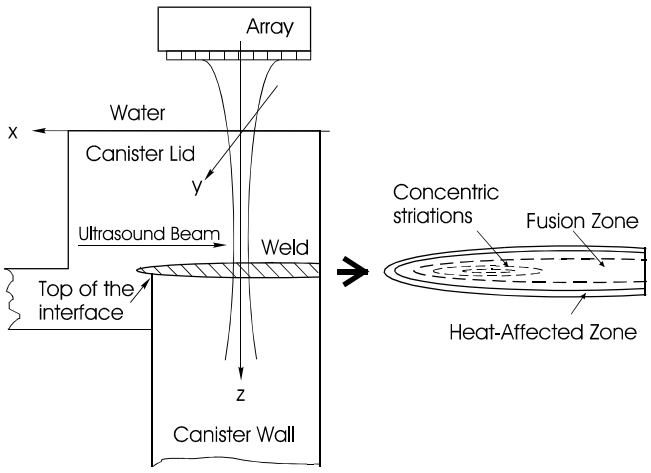

Fig. 5.1. Schematic of EB weld structure and of ultrasonic inspection of the EB weld.

The schematic of the EB weld structure and the inspection setup is illustrated in Fig. 5.1. A copper canister segment, block 3 of weld W123, was inspected. The ultrasound beam is normally incident on copper canister immersed in water. The beam was scanned electronically in the *x* direction and mechanically in the *y* direction. The data acquired in this way is 3 D, and, thus, can be displayed in A-, B- and C-scans. The B-scans (in envelope signals) are

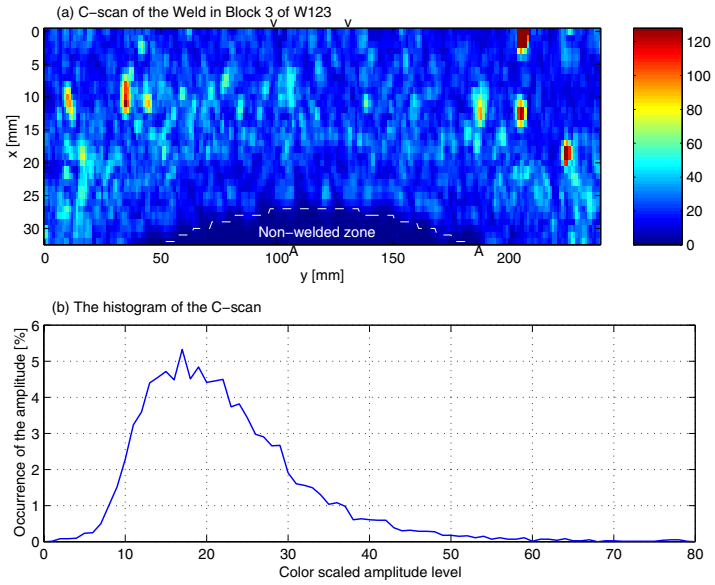

Fig. 5.2. The general C-scan of the EB weld in copper canister W123 and (b) the histogram of the C-scan with the non-welded zone excluded.

created by electronic scanning and extends in the *x* and *z* directions. The C-scans extend in the *x* and *y* directions.

A C-scan of block 3 of weld W123 is shown in Fig. 5.2, together with the histogram plot. The time window used for the C-scan covered the whole EB weld layer.

The B-scans of block 3 of weld W123 are shown in Figs. 5.3 and 5.4. The B-scan in Fig. 5.3 is a standard one containing the successive A-scans. Fig. 5.4 shows the B-scan processed with the spatial diversity method (see Chap. 6.2.2). In this processed B-scan the boundaries of the EB weld look smoother as well as more continuous because the grain noise has been largely reduced.

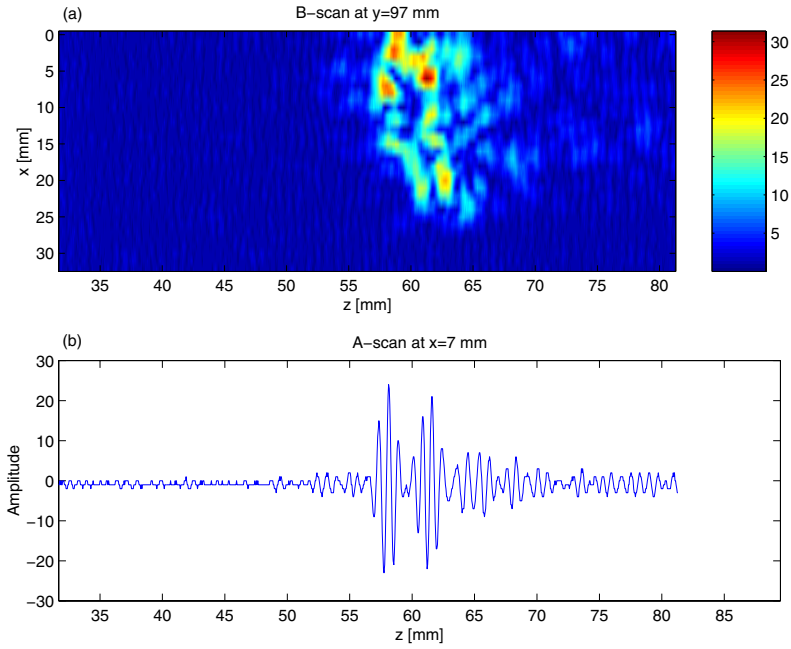

Fig. 5.3. The normal B-scan of the EB weld in Block 3 of Weld W123, located at *y*=97 mm in the C-scan in Fig. 5.2. (a).

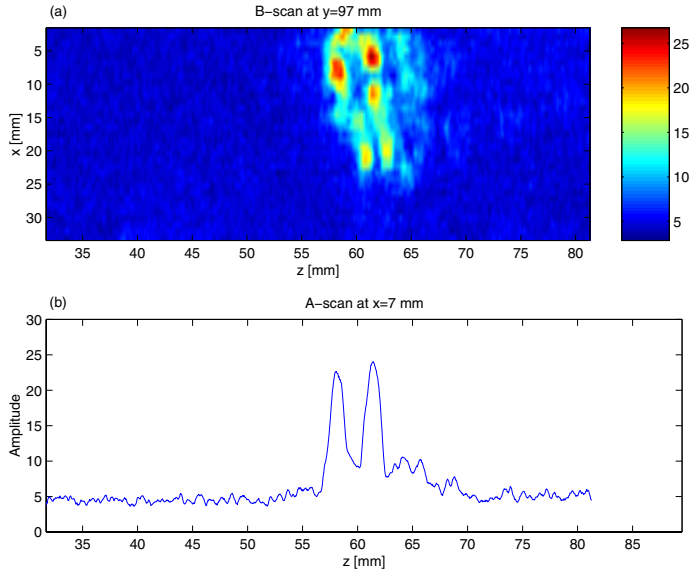

Fig. 5.4. The B-scan in Fig. 5.3 after processed with the spatial diversity method.

To depict the distribution of amplitude levels of ultrasonic scattering from the weld and host material a set of histograms were created from the local C-scans at depths from 50 to 81 mm below the top surface of the copper canister. The histograms that are presented at Fig. 5.5 show probabilities of different amplitudes indicated on the vertical axis as a function of depth z shown on the horizontal axis. The probabilities are shown in logarithmic color scale illustrated by the bar graph at the right-hand side of Fig. 5.5. The histogram in Fig. 5.5, when read vertically corresponds to the histogram at a given depth z. Three peaks corresponding to larger amplitudes that lie in the intervals of 55-60 mm, 60-65 mm, and 65-70 mm counting from the canister top, respectively, are well pronounced in the histogram. The first two peaks correspond to the strong scattered signals from the front and the back boundaries of the EB weld, and in between is a small valley, which means the low scattering from inside the fusion zone. The third peak results from the strong scattering by the top of the interface between the canister wall and the lid (see Fig. 5.1).

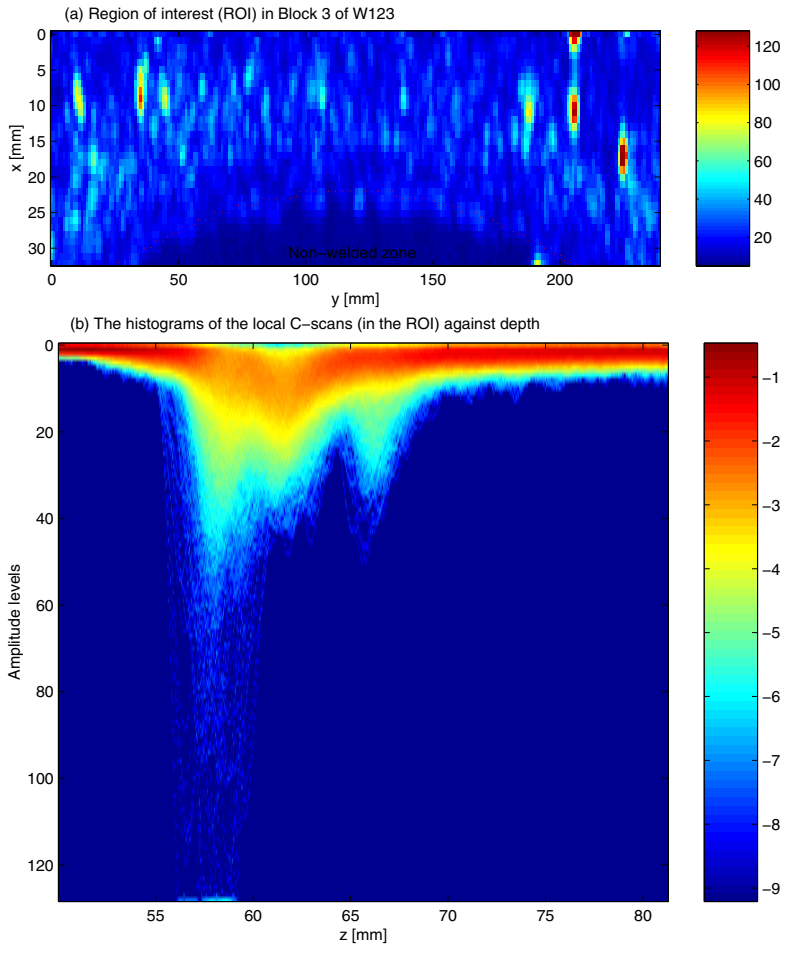

Fig. 5.5. In the region of interest (a), the histograms of the local C-scans in the region of interest are plotted against depth (b). Note that figure (b) is log compressed.

Using the three time windows that covered the depth ranges (a) from z=50 mm to 60 mm, (b) from z=60 mm to 65 mm, and (c) from z=65 mm to 70 mm, respectively, we extracted three C-scans shown in Figs. 5.6(a), (b) and (c). In Fig. 5.6(a) showing the upper boundary region, one can see most of the strong indications of flaws. In Fig. 5.6(b) showing the back boundary region, one indication is visible. In Fig. 5.6(c), the tip end of the canister inner wall can be seen and also one indication of possible tip flaw at x=26 mm and y=120 mm. It is apparent that a great deal of

useful information can be lost extracting a wide depth range C-scan in (compare Fig. 5.2 with e.g., the C-scan in Fig. 5.6(c)).

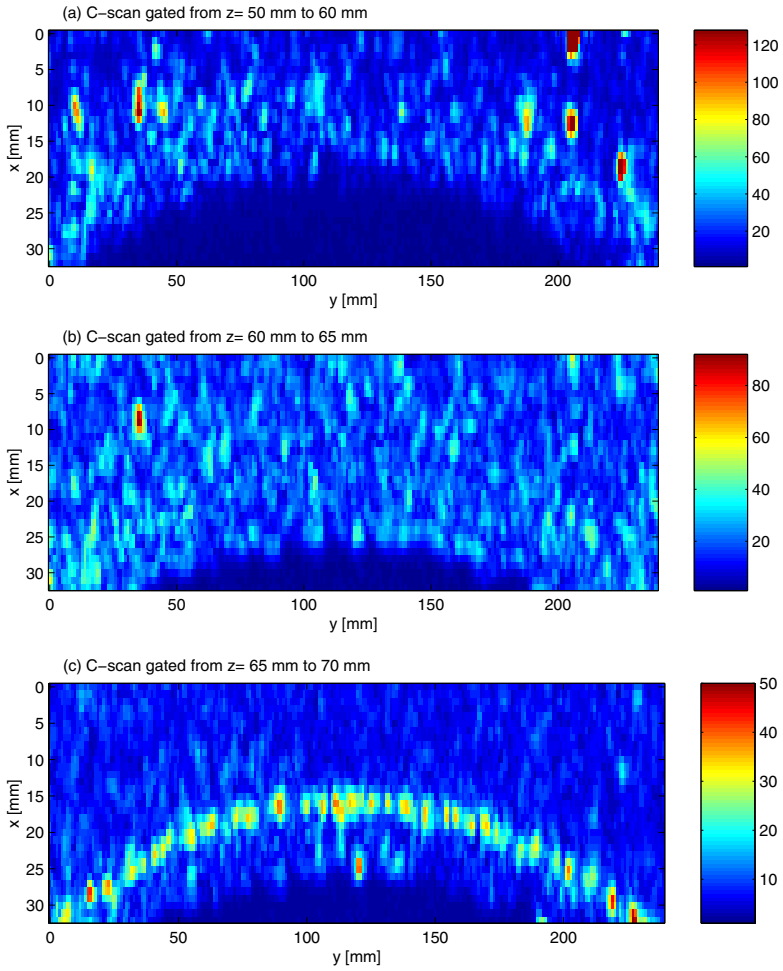

Fig. 5.6. The three C-scans gated by the three windows that cover the depth ranges (a) from z=50 mm to 60 mm, (b) from z=60 mm to 65 mm, and (c) from z=65 mm to 70 mm, respectively.

5.3 Ultrasonic imaging of EB welds using a multiple frequency transducer

As it was demonstrated above, C-scans yield an overall, top view of an EB weld and the dynamic range of scattered echoes. To examine the layered structure of an EB weld, the cross-sectional view that is shown in B-scan is helpful. Since the sizes of the grains in the weld zones (i.e., HMZ, HAZ and FZ), we used the three transducers of center frequencies of 2.3, 4.8 and 5.6 MHz together with the ALLIN system and inspected the copper canister block CAN 1. The first two transducers are the elements of the two-element annular array transducer designed for harmonic imaging (see Chap. 9), and the third one was Panametrics V315 with a measured center frequency of 8.6 MHz. The B-scans from those three transducers are shown in Fig. 5.7(a), (b) and (c), respectively. The horizontal axis in Fig. 5.7 is the scanning position y and the vertical axis is z-z_0 (where z_0 is the path length of the water layer), the depth in the copper block. Note that logarithmic scale of the signal envelope in these images used to highlight the weak scattering from the HAZ.

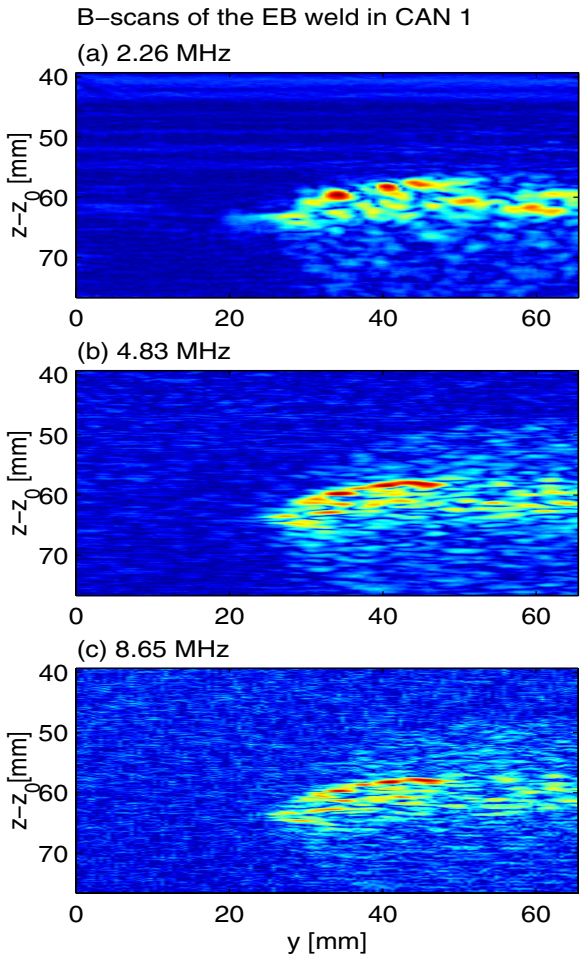

Fig. 5.7. B-scans of the EB weld in CAN 1 form the transducers with three different center frequencies: (a) 2.3 MHz, (b) 4-83 MHz, and (c) 8.6 MHz. Here z_0 is the water path length.

From these B-scans we can examine the cross-section of the EB weld. In each image a strip-like strong echo zone is seen that indicates the FZ within the region of y=0~42 mm, z- z_0 =56~64 mm. In the B-scan from the 2.3-MHz transducer the HAZ is very difficult to see. But the HAZ is easy to see in the B-scan from the 4.8-MHz transducer as well as the 8.6-MHz transducers (however, for the 8.6-MHz transducer the grain noise from the host material is more apparent and the electronic noise becomes larger). The reason for this is that the fine grains (in the HAZ) result in less scattering to the low frequency ultrasound than to the higher frequency one. From Fig. 5.7(b), the thickness of the HAZ can be measured as approx. 8 mm in the front part of the EB weld.

We can conclude that to inspect the HAZ of an EB weld, a transducer with higher frequency, e.g., 5 MHz, may be a good choice. To inspect the FZ, the transducer with lower frequency, e.g., 2~3 MHz (c.f., [17, 22]), can be a better choice. Combination of the inspections in the two frequency bands will give us more information on EB welds.

5.4 Ultrasonic velocity and attenuation in an EB weld

The ultrasonic velocity and attenuation in an EB weld were investigated based on the measurements made on the copper block CAN 1 using the 2.3- and 4.8-MHz transducers in Chap. 5.3.

5.4.1 Ultrasonic velocity

Because of the layered structure of an EB weld, the sound velocities in the host material zone (HMZ), the heat-affected zone (HAZ) and the fusion zone (FZ) are different. The difference in velocities in the host material and the EB weld can be seen in Figs. 5.8 and 5.9. In the figure the B-scans of the block front surface and the corresponding back surface are picked out, and shown respectively in panels (a) and (b) in Fig. 5.8 (from the 2.3 MHz transducer) and Fig. 5.9 (from the 4.8 MHz transducer). The straight stripes in Figs. 5.8(a) and 5.9(a) reveal that the echoes from the front surface at all scanning positions have almost the same phase fronts and the same frequency bands. Figs. 5.8(b) and 5.9(b) show the B-scans from the back surface from the two transducers. In these figures we can see two different regions. In the upper part (y=0~30 mm) where the EB weld is located, the stripes look rather straight and parallel. This may demonstrate that the sound speed in the weld zone is uniform. In contrast, in the lower part (y=35~65 mm) that is out of the weld zone, the stripes become bent towards the right hand side which indicates that the sound speed varies with position and the farther away from the weld (the larger the y coordinate) the lower the sound speed. The reason for this might be the gradient variation of heat effect of EB welding on a host material, which in turn results in different microstructure (e.g., grain size and elasticity) in the host material.

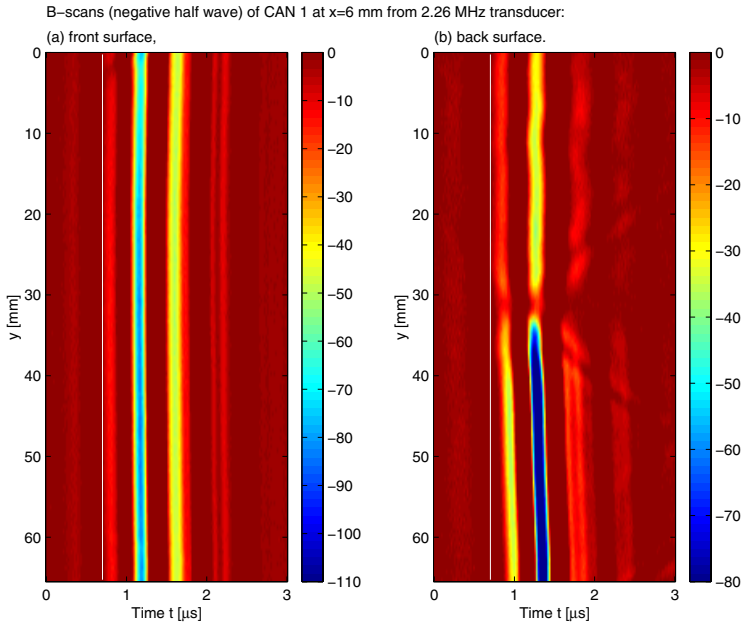

Fig. 5.8. B-scans of copper block CAN 1 from 2.3 MHz annular transducer with spherical focus (radius of curvature of 210 mm). (a) The front and (b) the back surface of the copper canister.

It is difficult to estimate

accurately the velocity in each zone. But it is possible to estimate the average velocity over the whole weld. The velocity can be estimated from the following relation,

$$V_w = 1 \Big/ \left(\frac{1}{V_c} - \frac{\Delta t}{2D_w} \right),$$

where V_w and V_c are the sound velocities in the weld and the copper block without welding, respectively. D_w is the weld thickness, and Δt is the time difference between the two copper blocks with the same thickness, one welded and the other without weld.

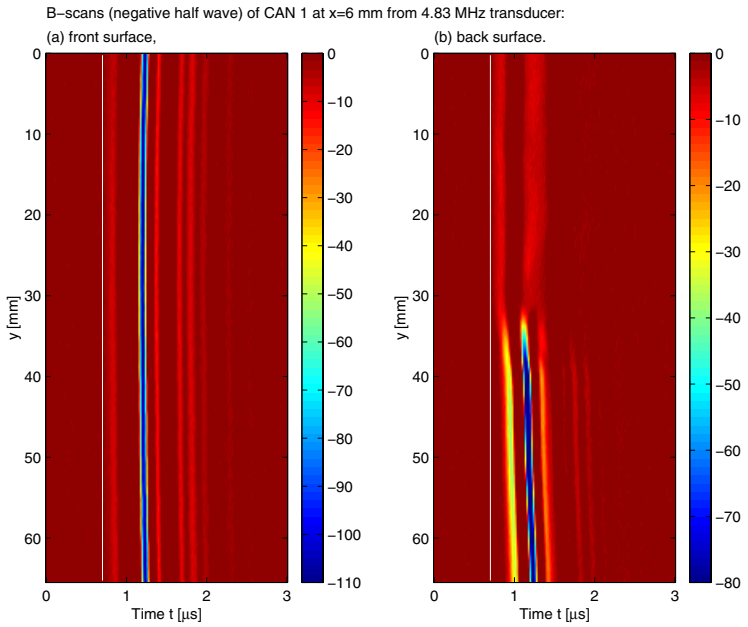

Fig. 5.9. B-scans of copper block CAN 1 from 4.8 MHz circular transducer with spherical focus (radius of curvature of 210 mm). (a) The front and (b) the back surface of the copper canister.

Comparing the A-scans in the welded area with those in the non-welded zone we can find their time differences and calculate their respective velocities. Assuming that parent material used both for the lid and wall of the copper canister has a sound velocity of 4596 m/s we obtain an average sound velocity in the EB weld of approx. 4674 m/s, which is 1.7% higher than that of its host material.

Difference and variation in sound velocities result in beam deflection. A significant difference in the sound velocities between the HAZ and the FZ results in well pronounced beam refraction and reflection at the boundary between the HAZ and FZ.

5.4.2 Ultrasonic attenuation

Attenuation in an EB weld is another important ultrasonic property. Quantitative estimation of the attenuation, especially the attenuation in each layer, is not an easy task. For example, grain size in an EB-welded copper canister may vary with positions in the host material, the HAZ and the FZ. Thus the thickness of each zone is difficult to accurately measure. However, it is possible to observe and estimate the excess attenuation of an EB weld by looking at the center frequency difference of the spectra of two echoes, one coming back through the EB weld and the other through the non-welded

zone. For the copper canister block CAN 1, we selected such two back echoes from the 2.3- and 4.8-MHz transducers, which are shown in Figs. 5.10(a) and 5.11(a), respectively, and found the center frequency differences for the two transducers (Figs. 5.10(b) and 5.11(b), respectively). These differences for two cases are 0.44 and 2.33 MHz, respectively, that correspond to 19% and 48% relative to the center frequency of the transducers. Obviously, the excess attenuation for the 4.8-MHz transducer is much larger. More accurate estimation of the excess attenuation can be made using the log spectral difference method.

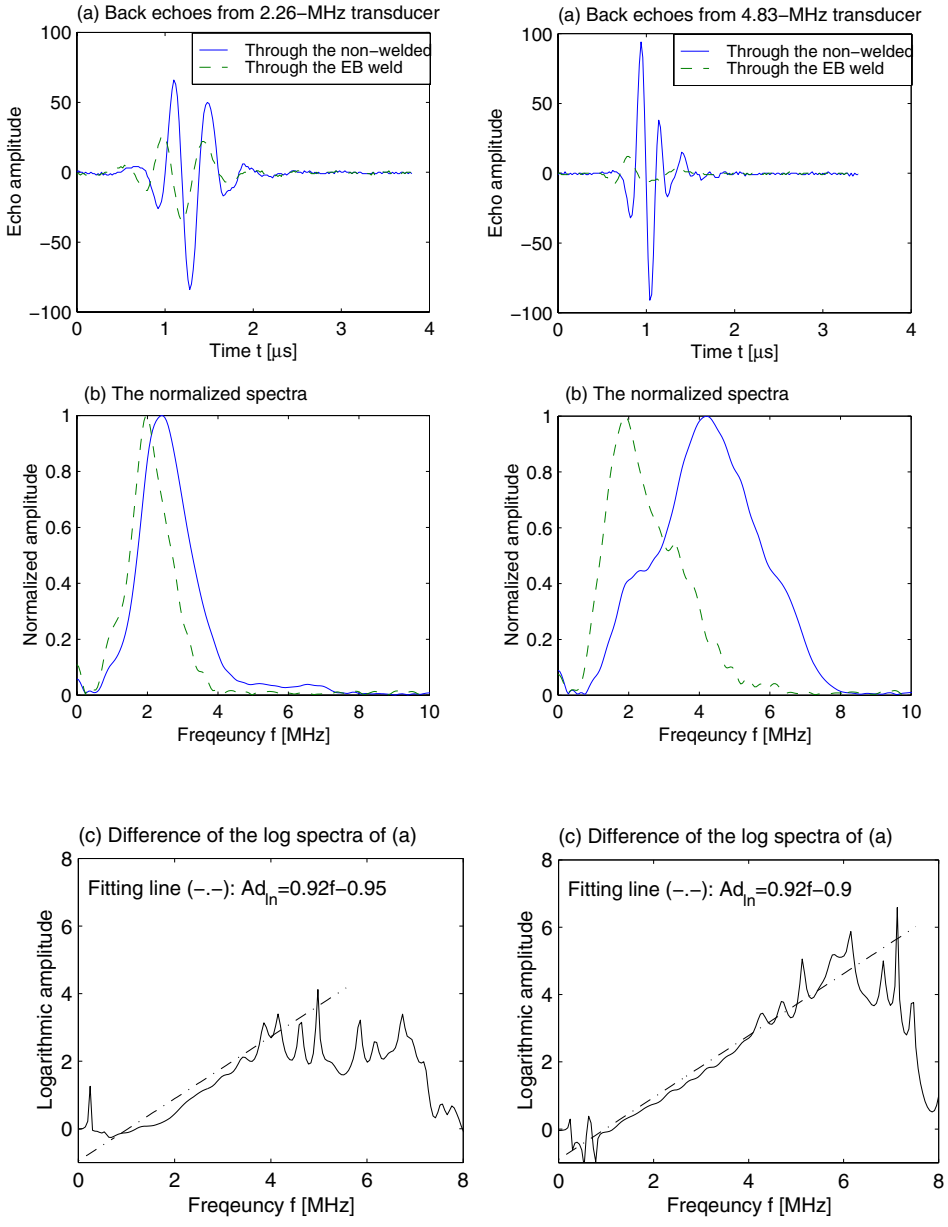

Fig. 5.10. (a) Back echoes from the 2.3-MHz transducer, (b) their normalized spectra, and (c) the difference of their log spectra.

Fig. 5.11. (a) Back echoes from the 4.8-MHz transducer, (b) their normalized spectra, and (c) the difference of their log spectra.

Taking the difference of the natural logarithms of the amplitude spectra of two back echoes, we have the excess attenuation against frequency for the two transducers (see Figs. 5.10(c) and 5.11(c), respectively). In Fig. 5.10(c) we can see a region from 1 to 4.5 MHz and in Fig. 5.11(c) from 1 to 6.5 MHz, over which the amplitude varies with frequency approximately in a linear manner. In such a "linear variation" region for each case, we find a fitting line, that is, $Ad_{\ln} = 0.92f - 0.9$ for the 2.26-MHz transducer (Fig. 5.10(c)) and $Ad_{\ln} = 0.92f - 0.95$ for the 4.83-MHz transducer (Fig. 5.10(c)). Both lines have the same slope 0.92 that will be used to estimate the excess attenuation.

The excess attenuation of an EB weld is given by [22]

$\Delta\alpha = \alpha_w - \alpha_c = (\alpha_{cw} - \alpha_c) \cdot D / D_w$,

where

α_c - the attenuation coefficient of the copper block without an EB weld,

α_{cw} - the attenuation coefficient of the copper block without and with an EB weld,

α_w - the attenuation coefficient of the EB weld including the reflection loss,

D - the block thickness, and

D_w - the EB weld thickness.

For CAN 1 that has the block thickness, D=79 mm, and the EB weld thickness, D_w=~10 mm, the excess attenuation of EB weld can be found to be,

$\Delta\alpha = \alpha_w - \alpha_c = 0.0458$ Np/(MHz · mm) $= 0.3997$ dB/(MHz · mm) .

For example, at 5 MHz, the excess attenuation is approx. 2 dB/mm, which is more ten times larger than that of a pure copper block with fine grains (e.g., 0.15 dB/mm at 5 MHz).

5.5 Conclusions

Evaluation of EB welds in copper canisters included the visualization of the structures of the welds, the analysis of from weld backscattering (grain noise), and the estimation of the velocity and attenuation in the weld.

An EB weld in a copper canister has been visualized from different angles by means of B- and C-scans. The B-scans gave cross-sectional views of an EB weld, and the C-scans offered top views of the weld at different depths.

Statistical analysis of backscattering (grain noise) from an EB weld was carried out based on the histograms of the weld ultrasonic images at different depths. From this analysis, a guideline for

selecting the time (or depth) windows for creating C-scans has been proposed. This guideline recommends using the following three windows (like for the C-scans in Fig. 5.6):

- the first one only covering the upper boundary of an EB weld,
- the second only spanning over the lower boundary, and
- the third covering the tip end of the canister's inner wall.

The above windows enable showing all the layers of an EB weld in more appropriate C-scans, and consequently, improve defect detection. For instance, the defects in the lower part of an EB weld are not any longer masked by the strong scattering from the upper part, which happens when only one time-window is used to cover the whole weld layer (like the window used for Fig. 5.2). From the C-scans created in this way, we have observed that the porosity tended to be concentrated towards the upper side of an EB weld.

Ultrasonic imaging of an EB weld using a multiple center frequency transducer has resulted in a significant improvement of imaging quality. The lower frequency transducer (2.3 MHz) produced B-scan with good contrast, which resulted in highlighting the FZ structure so that the upper and lower boundaries could be recognized. The higher frequency ultrasound from the 4.83-MHz transducer yielded good contrast for the HAZ above the FZ so that the HAZ became more apparent and easier to measure, but the back surface of the FZ became difficult to recognize. The combined inspections in the two frequency bands yielded more information on an EB weld.

The results from the study of sound velocity in an EB weld have shown that the average sound velocity in an EB weld was 1.7% larger than in the same material without weld. The difference of sound velocities in the EB weld and the host material would cause scattering, reflection, and refraction.

The study on ultrasonic attenuation in EB welds has revealed that the attenuation in an EB weld was much higher than in the host material. The studies on scattering and attenuation suggest that a suitable ultrasound frequency band for evaluating EB welds should be less than 5 MHz.

6 Processing Ultrasonic Signals

6.1 Introduction

The purpose of this task was twofold: First, to test the available algorithms for suppressing the backscattering from the weld structure that results in an ultrasonic noise limiting defect detectability. Second, to develop deconvolution algorithms for enhancing temporal resolution to improve defect imaging. The first aim is related to our previous research concerned with suppressing grain noise by means of linear and nonlinear filters. We have developed a number of nonlinear algorithms with split spectrum (filter bank) structure as well as linear algorithms using non-coherent detector concept. Those algorithms have been developed and verified previously for the ultrasonic inspection of welds in austenitic material encountered in nuclear power reactors. Our goal was to adapt those algorithms for the inspection of EB weld in copper and to verify them on the available canister samples. The deconvolution, which was the second signal processing aim, was performed using linear Wiener filters designed employing the available knowledge about system's impulse response.

It should be noted that the above-mentioned aims are quite interrelated, since the deconvolution enables reducing noise level in the C-scans (by taking narrower depth gate), and the successful noise suppression facilitates the deconvolution.

6.2 Algorithms for suppressing grain noise

The objective of this task was to investigate techniques capable of suppressing material (structure) noise backscattered from copper structure, especially in the EB weld zone. The level of material noise in the ultrasonic signal determines the ability to detect small flaws in the weld zone.

Material noise, backscattered from the irresolvable scatterers randomly distributed throughout the material is one of the main factors limiting imaging of flaws in metals. In copper canisters sealed with EB welds two noise patterns are encountered: the first, is in the solid copper used for lid and walls, and the second, is in the weld zone. The first pattern is typical for metals composed of randomly oriented anisotropic grains backscattering elastic waves. The second one is different since ultrasound is scattered both from the material grains and the weld structure which is characterized by certain regularity. Looking at the ultrasonic images (C-scans) obtained in pulse-echo inspection we can see a well-pronounced difference between the parent material and the welded copper; the weld structure

exhibits substantially more backscattering than the parent material. Although an image of ultrasonic backscattering from the EB weld can provide the operator with a very useful information about the weld structure, e.g., penetration depth of the electron beam and the flaws present in the weld (cf. our reports [6] and [7]), extracting information about the flaws when the weld noise is present requires special means and is generally a very complex task.

Techniques used for suppressing backscattering from the material structure utilize its inherent diversity resulting from the randomness of the irresolvable scatterers. They are based on the assumption that typical flaws due to their regular shape and significant size are characterized by relatively uniform pattern observed both in frequency domain as well as for different transducer positions in space. Thus, material noise can be reduced by some type of statistical operation performed on a set of diverse ultrasonic signals, either in frequency domain (*frequency diversity*) or obtained for different transducer positions (*spatial diversity*).

Generally, for increasing signal to noise ratio (SNR) we have to find and extract significant differences between the ultrasonic responses to defects and backscattering from the EB weld structure. This could possibly be achieved by some sophisticated filtering; wavelet, harmonic and matched filters were tested in this application without significant success.

6.2.1 Frequency diversity

Frequency diversity techniques that include different split spectrum processing (SSP) and specialized digital filters, such as noncoherent detector (NCD), are sophisticated filtering algorithms applied to ultrasonic signals stored in a digital form. It has been shown that when properly tuned, the algorithms can efficiently suppress grain noise in many practical applications [27].

It appeared, however, that these techniques are inefficient when applied to the signal from the EB weld zone in copper [11]. Our experiments performed on ultrasonic data acquired for different sections of canister weld have shown practically no reduction of backscattering from the weld zone after the SSP or NCD processing. This can be partly explained by the form of the ultrasonic signal reflected from the weld structure that appears to be similar to the reflections from the defects.

We can conclude that it appeared to be very difficult to distinguish between flaws and backscattering from the weld structure by frequency diversity technique using only one ultrasonic measurement obtained for a single focusing law of ultrasonic array.

6.2.2 Spatial diversity

The other approach mentioned above, *spatial diversity* is more elaborate since it requires several independent ultrasonic measurements obtained for different transducer positions to perform the statistical operation. Such measurements can be relatively easily performed using an ultrasonic array, for example by steering its beam at different angles and acquiring data from the same material volume for all those angles.

To test the spatial diversity concept we carried out two series of experiments: In the first experiment, EB weld was inspected by beams steered at different angles and focused in the weld. In the second experiment, responses of all individual aperture elements were acquired. The C-scans obtained in the first experiment [11] revealed considerable differences in the backscattered patterns obtained for various angles. Local intensity of the ultrasound backscattered from the weld structure was non-uniform over the C-scans. The individual C-scans were compounded using two methods, averaging and maximization. The averaging of the C-scans obtained for CAN1 reduced weld scattering and revealed round bottom holes that are hardly visible at normal beam incidence. However, other flaws are less pronounced comparing with normal beam C-scan.

Maximization consisted in comparing the amplitudes of the corresponding pixels in the individual C-scans and taking the maximal amplitude. This operation should result in an enhancement of all the strong scatterers observed at any angle. However, as a result the noise in the compounded image has also been intensified.

In the second experiment, the 32-element aperture was sending the pulse field 32 times at each scanning position, and for each pulse only one element was used to receive the backscattered ultrasound. In this way, the ultrasonic signals from 32 elements were obtained and acquired by the ALLIN system [17]. Since only one array element was used as receiver, the receiving sensitivity was much lower than that of a 32-element receiver.

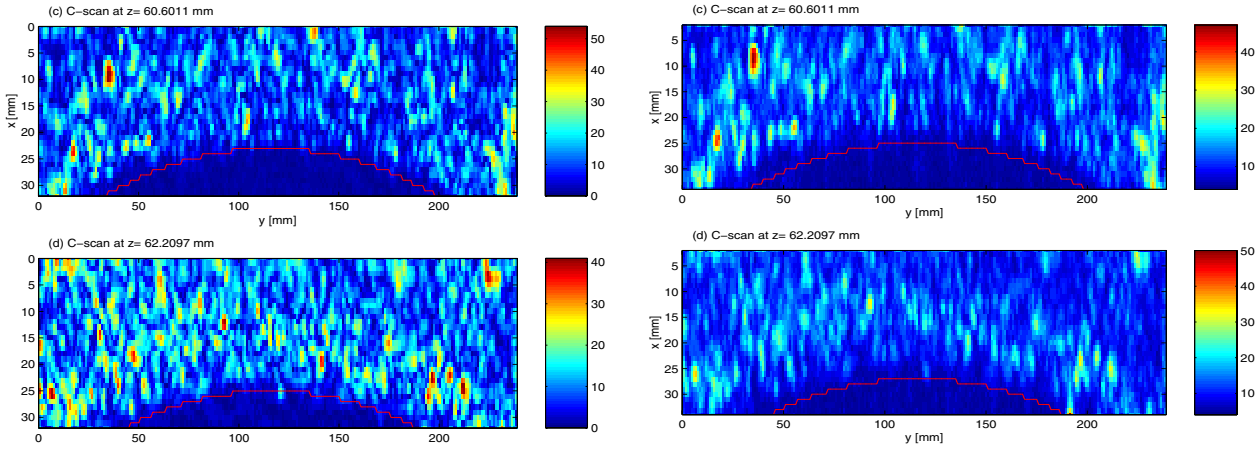

Fig. 6.1. Local C-scans at different depths (c) z =60.6 mm in the fusion zone, (d) z = 62.2 mm at the back boundary of the fusion zone. Raw data (left column), after spatial compounding (right column)

The acquired data were RF signals and could be used to create A- B- and C-scans either in a *phase-sensitive* way, or in a *phase-insensitive*. In the *phase-sensitive* compounding resulted in almost exactly the same C-, B-, and A-scans as those obtained in the conventional way. In the *phase-insensitive* way, the so-called spatial compounded data were obtained by summing up the envelope-detected signals from all 32 elements. The grain noise both in the weld parent material and in the weld has been suppressed as a result of phase-insensitive compounding, so that the C-scan images of an EB weld structure have been significantly improved (cf. Fig. 6.1).

6.2.3 Filtering algorithms

Wavelet filters designed using the continuous wavelet transform have been tested for different combinations of transducers and test specimens. Although some success has been observed for the filter based on sombrero wavelet [17] used for CAN1 specimen, the wavelet filters appeared to be inefficient in other cases [22].

Harmonic filtering was tested for the broadband signals obtained from an annular array generating a substantial amount of harmonic components. The filters used in this case had several pass-bands tuned to the successive harmonic components (comb filters). However, no significant improvement in SNR in C-scans was observed on specimen CAN1 [22].

Matched filters using 1D or 2D signal segment as a prototype were also tested [22]. In practice, the 1D matched filters did not influence the SNR. However, the 2D filters used for B-scans have shown an ability of reducing undesired signals, for instance, internal transducer vibrations, see Fig. 6.2.

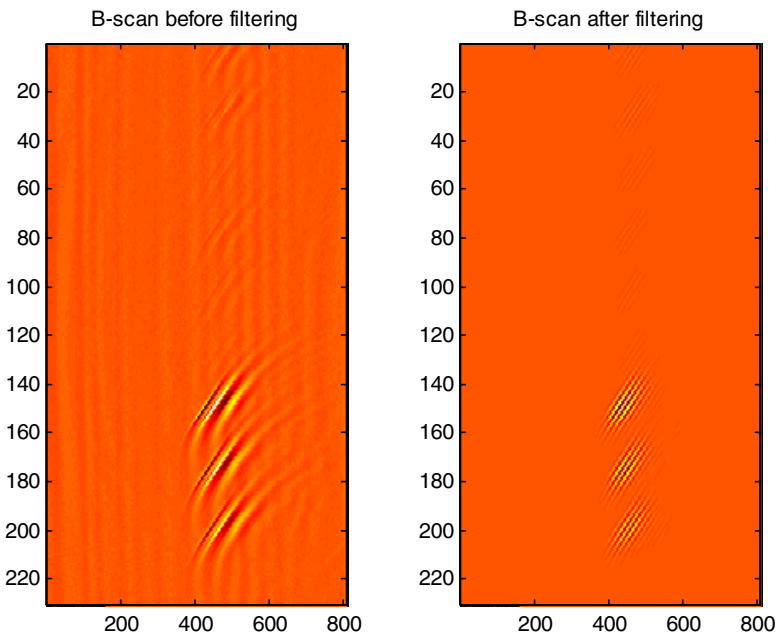

Fig. 6.2. B-scan of the 9 holes in CAN1 located in the EB weld before (left panel) and after (right panel) 2-D matched filtering. The matched filter using the area in green rectangle as a prototype also suppresses lower harmonic components in the signal. The vertical axis is in mm, and the horizontal axis is in samples.

To explain the lack of success using filtering algorithms a detailed analysis of ultrasonic signals received at different depths was carried out [22]. This analysis revealed that the back-scattered ultrasonic energy in the weld is non-stationary and very much dependent on the depth, which means that different filters should be used at different depths. An attempt with an adaptive matched filter did not yield any encouraging result [22].

6.2.4 Concluding remarks concerning the diversity algorithms

The general conclusion concerning both *frequency and spatial diversity was negative*. Experiments with frequency diversity techniques used for suppressing microstructure noise in the weld zone gave no improvement after processing ultrasonic data using algorithms that in preliminary tests had been capable of reducing grain noise in copper (parent material).

Spatial diversity approach performed by using steered beams with different angles, generated in an electronic way by the array resulted in variation of the backscattering pattern in C-scans obtained for different angles. Compounding by averaging was capable of suppressing random scattering but could also yield weaker signal from flaws if their response was dependent on the beam angle. Amplitude maximization resulted in enhancement of all scatterers including backscattering from the weld microstructure.

Spatial diversity obtained by compounding signals from the individual aperture elements yielded the desired reduction of grain noise at the price of a considerably increased inspection complexity and reduced spatial resolution. It should be noted however, that this latter price is not so significant in the focal zone.

Various filtering techniques designed to improve detectability of defects in EB weld zones have been tested without any spectacular success. It is worth noting that a fundamental requirement for the success of these techniques is the presence of a significant difference in ultrasonic responses from defects (voids) and weld clutter. This means that some spectral and/or phase difference between the signals due to detects and clutter should be extracted, otherwise the filtering fails to improve SNR.

The results from the filtering experiments indicate that the difference between the responses from the artificial defects and welds is *insufficient* to construct a good clutter suppressing filter of the type tested here, and the gain in terms of signal-to-noise ratio is, therefore, not dramatic after processing.

However, filtering had some positive effects, for example, applying 2-D matched filters to the images removed the unwanted, low frequency oscillations coming from the transmitter and smoothened the images. Even the C-scan image quality could be slightly improved without loosing spatial resolution.

6.3 Enhancing the temporal resolution

The amount of clutter observed in an ultrasonic signal depends on the geometry of transducer beam. Due to the transducer integrating action the level of clutter depends on the beam cross section, the more focused is the beam the fewer grains are illuminated and contribute to the scattering. In other words, clutter level depends on the spatial resolution of the used transducer. Similar situation is observed for the temporal resolution, high resolution enables resolving closely spaced grains in the ray direction and obtaining C-scans with lower level of clutter. This means that the resolution enhancement results in reducing amount of clutter in ultrasonic images.

Temporal resolution may be enhanced directly by using shorter wavelengths or indirectly by filtering techniques known as *deconvolution*. The deconvolution operation does not change any physical parameters of the ultrasonic waves; it is used for compensating the band-pass frequency response of the transducer used for the inspection. The success of the deconvolution depends on the amount of knowledge about the transducer, more precisely, the knowledge of the transducer response to the particular types of defects (e.g., cracks, voids, etc.). It is also important that the ultrasonic signals that are to be deconvolved have the widest available bandwidth. The deconvolution can be thought of as an inverse filtering of the ultrasonic data to remove, or at least decrease, the influence of the measurement system. Wiener filter is the classical method of deconvolution [28].

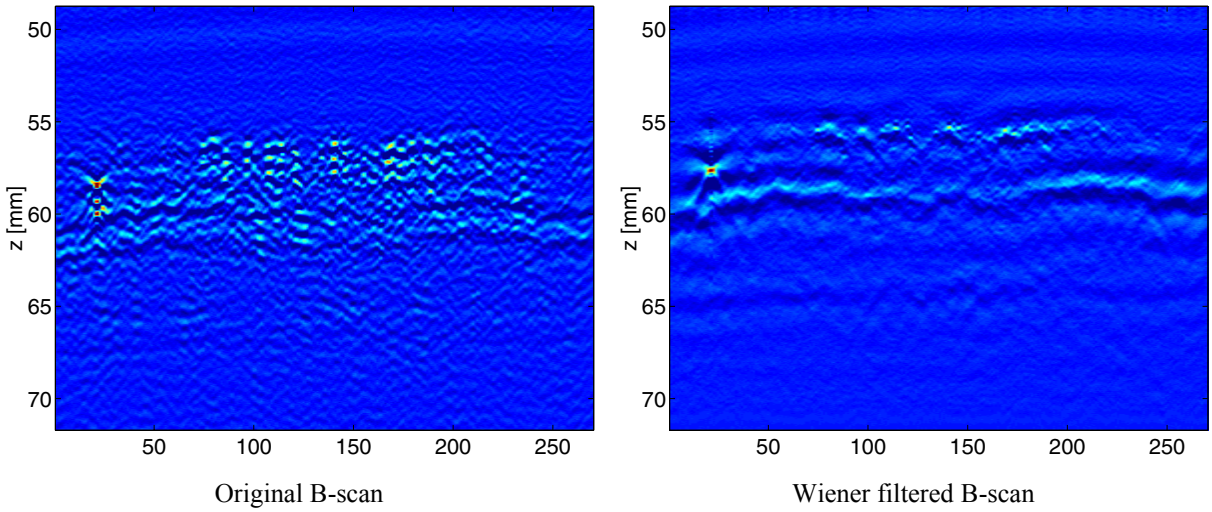

Fig. 6.2. B-scan images from the CAN1 specimen before and after Wiener filtering. Echoes from the drilled holes are visible in the upper part of the scans (yellow-red dots). Parallel reflections from different zones are very well pronounced after Wiener filtering.

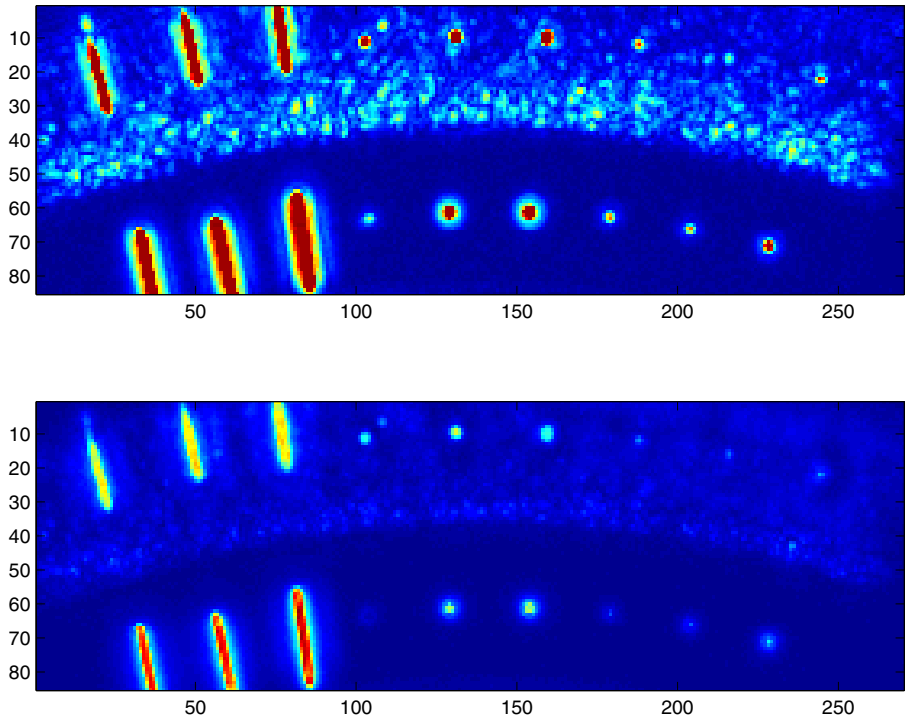

Fig. 6.3. C-scan example from the middle part of the weld in CAN1 before (upper panel) and after Wiener filtering (lower panel) using the 2.3-4.8 annular array. The vertical (y) and horizontal (x) axes are both in mm.

The effects of Wiener filtering were studied using signals acquired with the 2.2-4.8 MHz annular array on the specimen CAN1 [22]. This array is very well suited for the job due to its wide frequency band (due to the transmitter harmonic components received by the receiver) [24].

The results, after processing the US data with a Wiener filter, show a substantial improvement in temporal resolution (cf. Fig. 6.2). It is much easier to see the layered structure in the weld after processing, which facilitates the interpretation of the measured data. The C-scans extracted from the deconvolved US data exhibit a significantly improved SNR (cf. Fig. 6.3). The degree of improvement depends on the flaw location, the best success is observed for flaws located in the upper part of EB weld, above the strong scattering layer.

6.4 Summary and conclusions

Development of signal processing has been carried out with the aim to refine ultrasonic imaging and to perform better weld clutter suppression. Various filtering techniques have been designed to improve detectability of defects in EB weld zones. The techniques such as split spectrum processing, noncoherent detection, matched filtering, wavelet and harmonic filters have been investigated. A general conclusion that can be drawn from the experiments conducted using the available specimens is that *the signal processing does not yield a substantial reducing of clutter leading to the improvement of the SNR*. A common requirement for the success of these techniques is the presence of a significant difference in ultrasonic responses from defects (voids) and weld clutter. The results from the filtering experiments indicate that the difference between the responses from the artificial defects and welds is insufficient to construct a successful clutter suppression algorithm of the form used here. *However, filtering may have some positive effects*, for example, the 2-D matched filters removed the unwanted, low frequency oscillations generated by the transmitter and smoothened the images.

Experiments with two types of spatial diversity have shown that this technique is capable of reducing clutter amount in the C-scans. However, the improvement is obtained at the price of increased measurement complexity and some reduction of spatial resolution.

The time resolution is another important issue in US evaluation of EB welds. Poor resolution means that the US responses to different scatterers are smeared, which impairs the quality of C-scan imaging. Therefore, deconvolution has been implemented in order to remove, or at least decrease, the smearing that the measurement system induces. The classical Wiener filtering used for deconvolving the US data yielded a substantial improvement in temporal resolution. The layered structure in the weld was much better pronounced after the processing, making the interpretation of the US data much easier. *The deconvolution, performed using Wiener filter enabled also extracting C-scans with a significantly improved SNR*.

7 Harmonic imaging

7.1 Introduction

Harmonic imaging technology (HIT) has emerged as a major imaging trend in medical ultrasound that has enabled a substantial improvement of the image quality in medical ultrasonic imaging. In an attempt to exploit the HIT for the NDE purpose an experimental study has been conducted.

We have exploited two types of harmonics for harmonic imaging (HI) of materials: (i) transducer harmonics that originate from the high order resonant modes of a transducer excited with a broad band signal, and (ii) material harmonics that result from the nonlinear propagation of ultrasound in materials.

The overall purpose of the research on harmonic imaging is to expand the existing space of ultrasonic imaging technology used in nondestructive evaluation (NDE) through exploring the information on materials and defects that may be contained in harmonics. The goals of the present work are rather general: Firstly, to make the best use of information (including transducer harmonics) contained in ultrasonic signals received by wide band receivers. Secondly, to investigate experimentally the nonlinear phenomenon of elastic wave propagation in solids. Thirdly, to show the possibility of applying the harmonic imaging technology to the NDT.

7.2 Transducer harmonic imaging

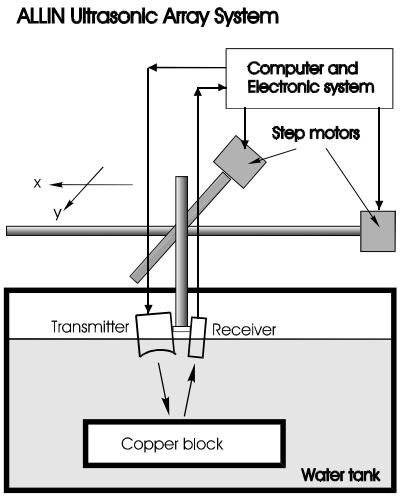

Fig. 9.1. Experimental setup for transducer harmonic imaging.

Transducer harmonic imaging employs harmonic components from the high order resonant modes of transducers to construct images. This study has two particular aims: investigating the feasibility of basic harmonic imaging technique, and developing a signal processing technique for improving the signal-to-noise ratio. The experimental setup used for this study is shown in Fig. 7.1. The transmitter used was a broadband, spherically focused transducer (PANAMETRICS V392) that had a 0.85-MHz center frequency (measured), an 87% –6-dB bandwidth. The receivers used with the transmitter in different configurations were four broadband planar transducers (PANAMETRICS V325, V383, V326 and V327) that had nominal center frequencies of 2.25, 3.5, 5, and 10 MHz, respectively.

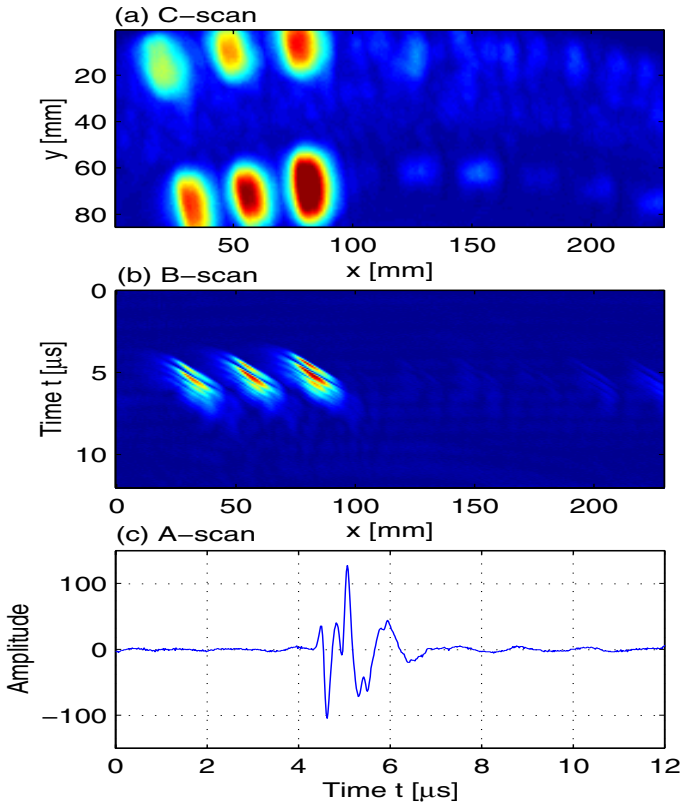

Fig. 7.2 C-, B- and A-scan from the measurement made on the copper block using the 1-MHz focused transmitter and 7-MHz planar receiver. (a) C-scan, (b) B-scan at y=72 mm, and (c) A-scan at x=56 mm and y=72 mm that comes from the side-drilled hole, SDH #11.

Copper block CAN 1, containing an EB weld, and a set of side-drilled holes and bottom-drilled holes was inspected with each of the above mentioned transmitter/receiver pairs.

The 3D RF data that can be used to create the A-, B- and C- scans of the copper block has been acquired for each transducer pair. An example is shown in Fig. 7.2 in which the C-, B- and A-scan come from the measurement made on copper block CAN 1 using the 1-MHz focused transmitter and the 7-MHz planar receiver. The C-scan in 9.2(a) was obtained using the gate selecting the whole EB weld. The B-scan in 9.2(b) shows the cross-sectional view at y=72 mm in the C-scan. The A-scan in 9.2(c) is at x=56 mm in the B-scan, and the echo comes from the side-drilled hole # 11 (see chapter 7.3). It is worth noting that although the captured harmonic components may contain some material harmonics, the latter ones are small in this case, which will be explained in the next section. Each harmonic component was extracted using a Hanning window for filtering the spectra. The filtered A-scans were then used for extracting C-scans in a conventional way (detecting a maximum signal amplitude in a certain depth range). An example of such a C-scan is presented in Fig. 7.3.

From our examination and analysis it appears that the spatial resolution increases with the order of harmonic component, i.e., the higher order harmonic gives the better spatial resolution at the price of increased noise level. The observed resolution improvement agrees with the theory since the higher harmonic components correspond to the shorter wavelengths.

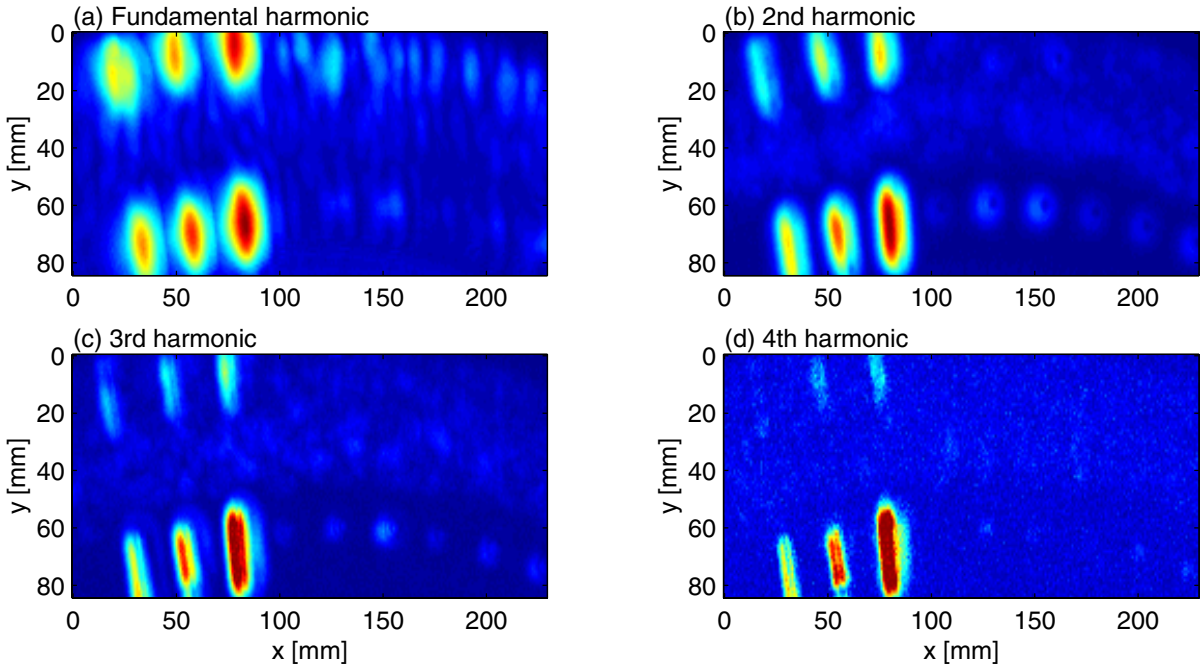

Fig. 7.3. C-scans (a)– (d) constructed from the fundamental to the forth components, respectively, in the case of using the transmitter and receiver pair, T/R: 1/7 MHz.

7.3 Material harmonic imaging

7.3.1 Experimental setup

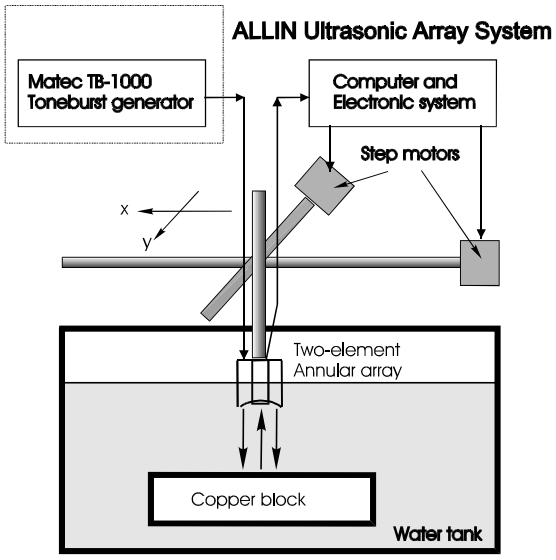

Fig. 7.4. Experimental setup for material harmonic imaging.

For this study we have designed a special transducer, a two-element array transducer that has two spherically concentric elements (see Fig. 10.3 for details). The inner element is circular with a 4.8-MHz center frequency and a 73% bandwidth while the outer element is annular and has a 2.3-MHz center frequency and a 69% bandwidth. The two transducer elements were used in pitch-catch mode, that is, the outer element was used as transmitter, and the inner one with higher frequency was used as receiver. The experimental setup for the study is schematically shown in Fig. 7.4.

To avoid transducer harmonics and to get material

harmonics, we excited the transmitter with a narrow band excitation, a tone burst, whose frequency was 2.15 MHz that was close to the transmitter center frequency. The tone burst was created by the tone burst card TB-1000 made by Matec and applied to the transmitter (the outer element). The receiver (the inner element) was connected to the ALLIN system that implements signal amplification, mechanical scanning, and data acquisition.

This study has been conducted systematically in the following steps: first of all the frequency spectrum of the tone burst exciting the transmitter was selected so that only the fundamental resonant mode was excited. Then, material harmonics were examined in water, in a copper block with a set of side-drilled holes at different depths (Cu 2), and finally, in copper canister block CAN 1. The two copper blocks were inspected in immersion configuration, as shown in Fig. 7.4.

7.3.2 Harmonic generation in water

Nonlinear acoustic waves in water were examined. The measurements were made on and off the axis at different positions. The echoes and their spectra obtained at z=135 and 155 mm on the axis are shown in Fig. 7.5. All the spectra in Figs. 7.5(e´) and (f´) were normalized to facilitate the comparison of the higher harmonics with fundamental components. The echoes in Figs. 7.5(e) and (f) show to be seriously nonlinearly distorted in comparison with the original tone burst.

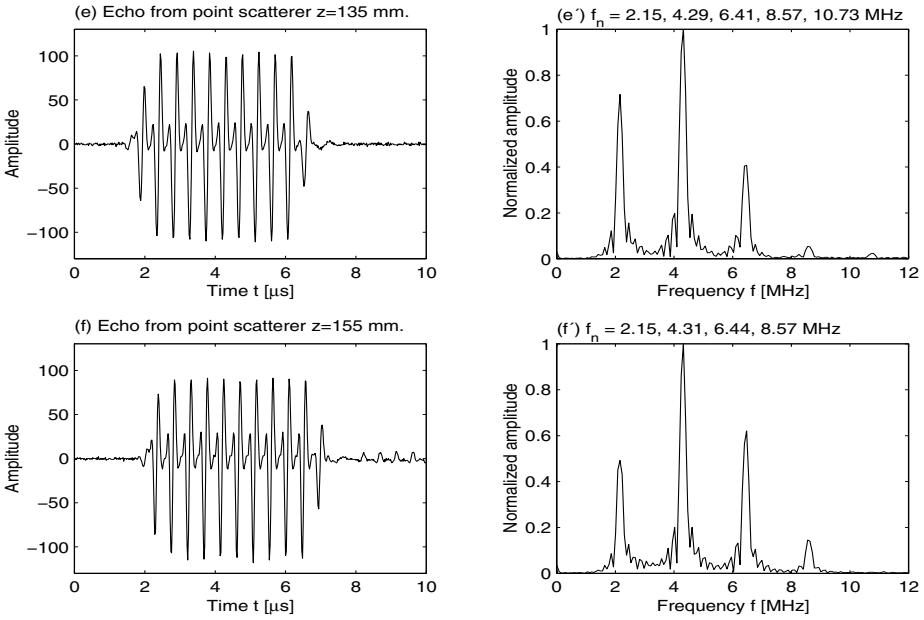

Fig. 7.5. Pulse echoes from a point scatterer on the transducer axis at distances (e) z=135 mm, and (f) z=155 mm. (e´) and (f´) The spectra of the pulse echoes in (e) and (f).

These nonlinear distortions are shown to be a series of higher harmonics in the frequency domain, e.g., in Figs. 7.5(e´) and (f´) we can clearly see not only the fundamentals at 2.15 MHz, but also

higher (2nd – 4th) harmonics at about 4.30, 6.42, and 8.57 MHz, respectively. Referenced to the fundamentals in the spectra shown in Figs. 7.5(e´) and (f´), one can see that the high harmonics (e.g., 2nd – 4th harmonics) increase when the distance to the focal point (210 mm) decreases.

7.3.3 Harmonic imaging of the EB weld in copper block CAN 1

Harmonics in copper canister block CAN1 were generated with the same experimental setup (Fig. 7.4), and then used to construct the harmonic images of the EB weld in the canister.

A series of measurements were made on CAN 1 using the two-element transducer. The transmitter was excited with a tone burst consisting of 12 sine cycles, at frequency 2.15 MHz. The receiving transducer was connected to the TB-1000's amplifier and then to the ALLIN system.

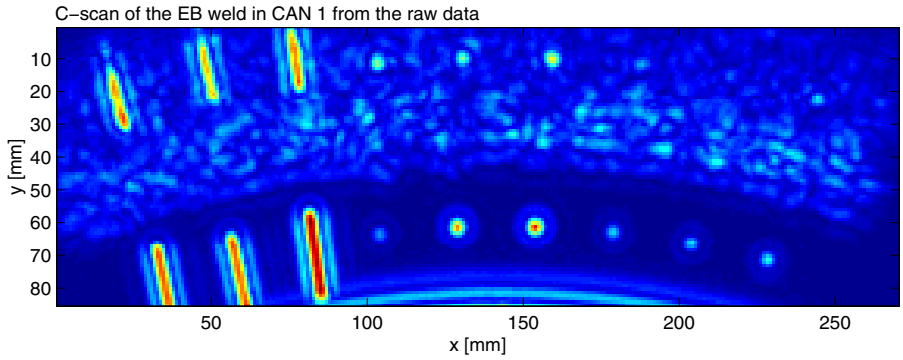

Fig. 7.6. C-scan of the EB weld in CAN 1 from the raw data.

A series of measurements were made using different amplitudes of the transducer excitation (both low and high) and different settings of the high- and low-pass filters of the TB-1000 amplifier. The C-scan shown in Fig. 7.6 was extracted from the acquired data using a time gate covering the whole EB weld. From the C-scan we selected the following four representative positions of interest: SDH #3, FBH #6 and two EB weld spots. The A-scans at these positions are shown in Fig. 7.7 together with their log spectra. In the spectra of the SDH #3 and FBH #6 echoes (Fig. 7.7(a') and (b')), the second and third harmonics (at ~4.30 and 6.42 MHz, respectively) are clearly visible, and the fourth (at ~8.60 MHz) is weakly pronounced in the SDH #3.

Moving to the echoes from two EB weld spots (Fig. 7.7(e) and (f)) and their spectra (Fig. 7.7(e') and (f')), we see that the nonlinear distortion in this case is still apparent. The 2nd and 3rd harmonics are clearly there, although smaller than for the echoes from SDH#3 and FBH#6.

Using Hanning widows with center frequencies being the same as the harmonics to the spectra, we have extracted the fundamental and the 2nd – 4th harmonics and constructed A-, B- and C-scans for all of them. Here we present only the C-scans of the fundamental and the second harmonics (Fig. 7.8).

The fundamental C-scan of the EB weld, extracted from the measured data (when the low- and high-pass filter were not used) is shown in Fig. 7.8(a). Since the fundamental component is dominant, this fundamental C-scan looks very similar to the one in Fig. 7.6. The 2nd harmonic C-scans in Fig. 7.8(b) was obtained from the data measured with the 5-MHz high-pass filter (four A-scans used for this C-scan are displayed in Fig. 7.7). All the SDHs (#1-#3 and #12-#15) and the FBHs (#13-#18) in the non-welded zone are seen both in the fundamental C-scan and in the 2nd harmonic C-scan.

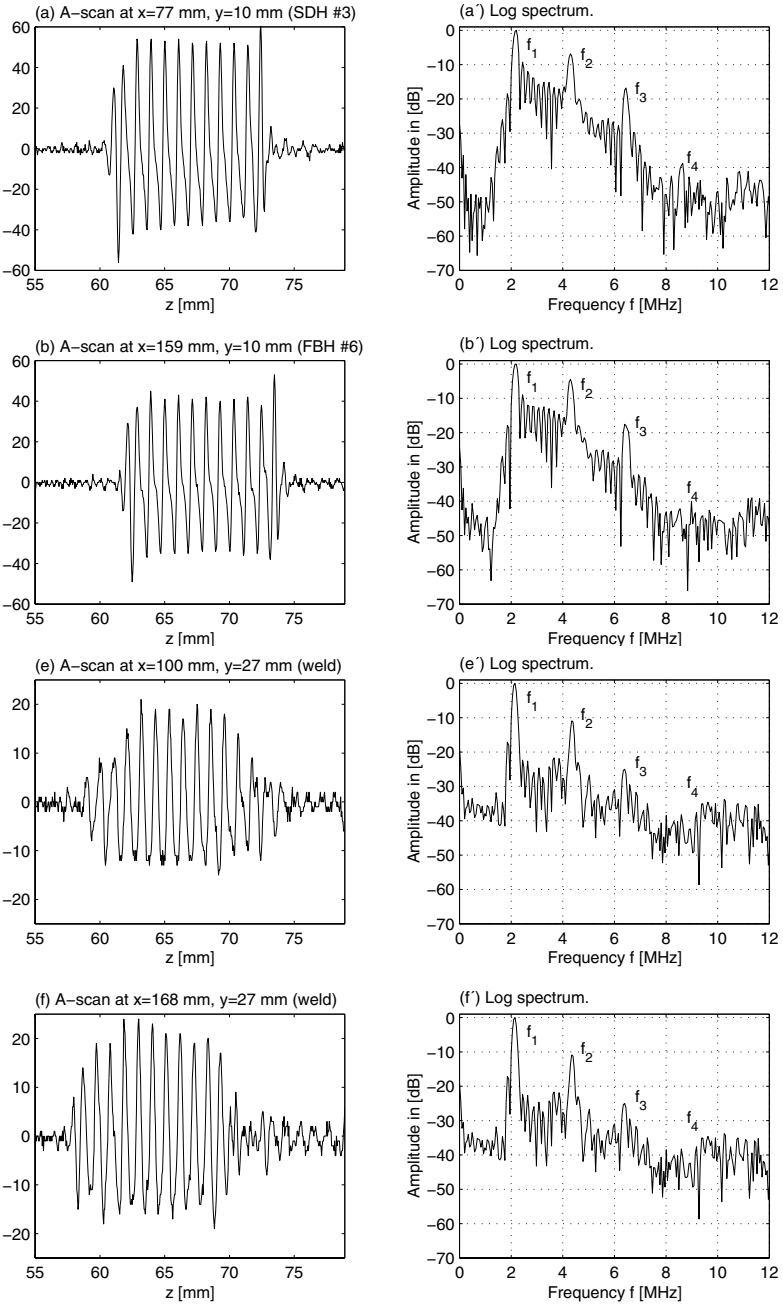

Fig. 7.7. A-scans at positions (a) x=77 mm, y=10 mm (SDH #3), (b) x=159 mm, y=10 mm (FBH #6), (e) x=100 mm, y=27 mm (weld), and (f) x=168 mm, y=27 mm (weld).

Comparison of the hole images in the C-scans in Fig. 7.8 reveals that the spatial resolution becomes better for the higher-order harmonic image. Observation of the grain noise may allow us to say that the grain noise pattern becomes finer for the higher-order harmonic.

The above presented observations and analysis have confirmed that it is possible to generate harmonics in an EB weld and revealed that harmonic imaging of EB welds is feasible.

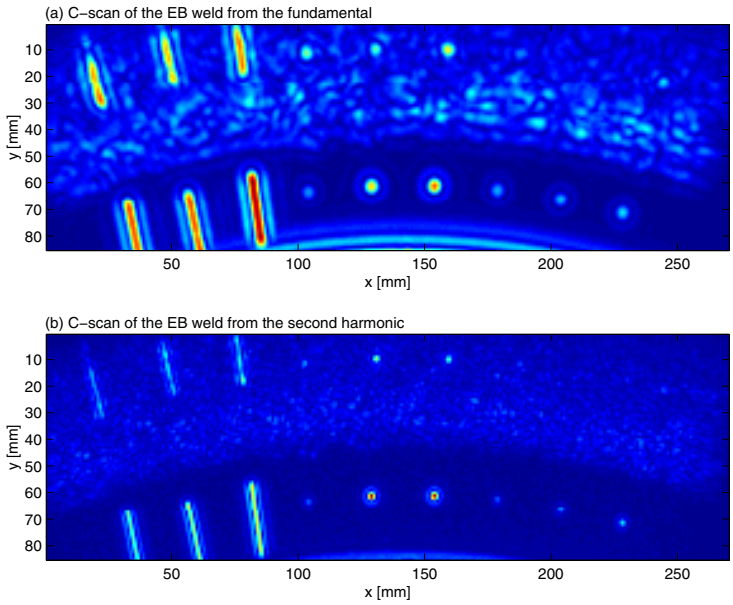

Fig. 7.8. C-scans of the EB weld in CAN 1 from (a) the fundamental, and (b) the second.

7.4 Conclusions

Harmonic imaging of EB welds has been studied by exploiting two different sources of harmonics. The first one was referred to as transducer harmonics that originated from the high-order resonant modes of transmitters excited by a broadband pulse, and the second one was called material harmonics that came from the nonlinear distortion of waves propagating in materials.

The transducer harmonic imaging technique exploits additional information due to transducer harmonics. The results from the study show that the higher harmonic imaging had a better spatial resolution. The observed resolution improvement agrees with the theory since the higher harmonic components have the shorter wavelengths.

The material harmonic imaging has been conducted in a systematic way. The harmonic generation has first been made in water. Strong nonlinear waves in water have been observed and the harmonics up to fifth order showed up. Then the experiments were conducted on copper block, and the results have shown the presence of harmonics up to fourth order. Finally, the harmonic generation was made in a copper canister CAN 1 with an EB weld. The harmonics up to third order from the EB weld have

been clearly seen, and the fourth harmonic from some artificial defects were also visible. The ultrasonic images (C-scans) of the fundamental, and the higher harmonics have been extracted. From this experimental study, we can conclude that the spatial resolution becomes better and the grain noise pattern becomes finer for the higher-order harmonic image. Further exploration of nonlinear elastic waves and advancing the materials harmonic imaging technique for ultrasonic NDE seem be promising and stimulating, similarly as the tissue harmonic imaging technique in medical ultrasonography has resulted in significant improvement in image quality.

8 Beam forming – focusing and steering

8.1 Introduction

The ALLIN ultrasonic array system possesses the capacity of performing beam forming, i.e., beam focusing and steering. Different beams are useful for different purposes. Focused beams can improve lateral resolution of ultrasonic imaging of EB welds. Steered beams are used to inspect the regions close to canisters outer walls because the normal beams have difficulties in accessing these regions. Usually, the steered beams are also focused. Beam forming is implemented by designing delay times (often called focusing laws) and apodizations for the array elements used in an aperture.

The purpose of this task was to develop a tool for designing the focusing laws for the ALLIN array that would enable generating optimal steered and focused beams in immersed copper canisters. The tool was created using theory of geometrical acoustics.

8.2 Theory

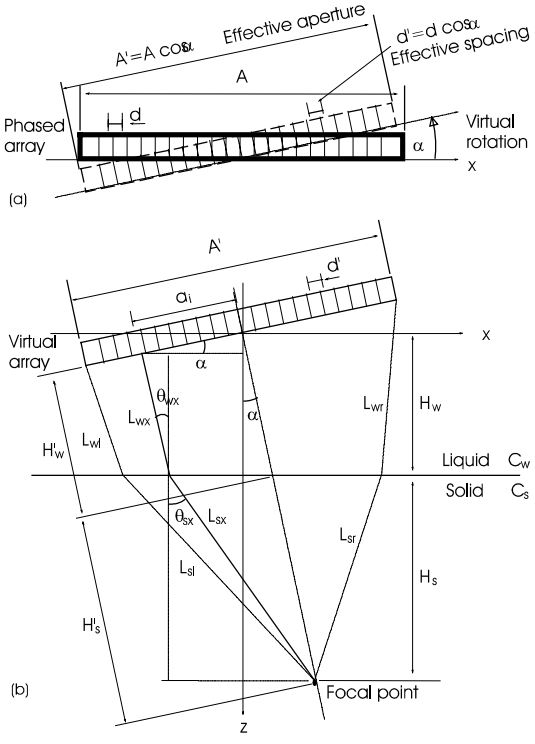

Fig. 8.1. Geometry and notation for the calculation of delays used for the phased array to steer and focus a beam in an immersed solid.

Consider a phased array consisting of N' elements with size $2a \times 2b$ and spacing d, located in a fluid at plane $z = 0$. We desire such a beam that is steered at angle α and still focused at point F as if there were no refraction at the interface (see Fig. 8.1(b)). Such a solution is very desirable from the practical point of view as it can simplify imaging of targets detected in the immersed solid.

To obtain this steered, focused beam, we will take two steps to figure out the delays. Firstly, the beam is steered by angle α by applying the following delay time sequence to the voltage pulses to the array elements,

$$\tau_{si} = (i - 1/2)d \sin\alpha / c, \qquad (8.1)$$

where i = -N'/2+1, ..., 0, 1, ... N'/2. The array that steers a beam by α is virtually rotated from the physical array by α (see Fig. 8.1(a)) and has the

effective aperture length $A' = N' d \cos\alpha$ and the effective spacing $d' = d \cos\alpha$. In sequel, the virtually rotated array is called virtual array having the effective aperture length A' and the effective spacing d'. Secondly, based on this virtual array, set the focal point at position F, and calculate the delay times for the focus, τ_{fi}. The delay time τ_{fi} for the ith element of the *virtual array* is calculated based on geometrical acoustics in such a way that all acoustic pulses coming from the centers of the elements should simultaneously arrive at the desired focal position (see Fig. 8.1(b)).

We assume that the distance from the virtual array's center to the fluid/solid interface is H_w and the distance from the fluid/solid interface to the focal point is H_s. The focal length is $H'_w + H'_s$, where $H'_w = H_w / \cos\alpha$ and $H'_s = H_s / \cos\alpha$. The delays for focusing are determined by

$$\tau_{fi} = \frac{L_{wr} - L_{wx}}{C_w} + \frac{L_{sr} - L_{sx}}{C_s} = \frac{1}{C_w}\left(\frac{H_w - A'\cos\alpha/2}{\cos\theta_{wr}} - \frac{H_w - a_i\cos\alpha}{\cos\theta_{wx}}\right) + \frac{H_s}{C_s}\left(\frac{1}{\cos\theta_{sr}} - \frac{1}{\cos\theta_{sx}}\right) \quad (8.2)$$

where θ_{sx} and θ_{wx} are found by solving the following two equations

$$\tan\theta_{sx} = \frac{a_i(\cos\alpha + \sin\alpha\tan\theta_{wx}) - H_w\tan\theta_{wx} + (H_w + H_s)\tan\alpha}{H_s}, \quad (8.3)$$

$$\sin\theta_{wx}/C_w = \sin\theta_{sx}/C_s \quad (8.4)$$

Finally, the total delay times τ_i applied to the ith element of the array (not the virtual array!) for the desired beam is obtained simply by summing the delay times for steering and focusing,

$$\tau_i = \tau_{si} + \tau_{fi}. \quad (8.5)$$

It should be pointed out that the delays obtained from Eq. (8.5) can be both positive and negative, e.g., for a steered beam as in Fig. 8.1(b) the delays are positive for the array elements at $x>0$ and negative for those at $x<0$. In practice, however, the delays should be all positive. Thus, all the delays must be added by a certain positive value so that they all become nonnegative.

The focusing law determined by Eq. (8.2) in the immersion case is no longer cylindrical as in the case of a homogeneous medium. This type of focusing is called *optimal* focusing.

8.3 Conclusion

A tool (a computer program) for designing the delay times (focusing laws) for the ALLIN array (as well as other linear arrays) to produce optimal steered, focused beams in immersed solids (immersed copper canisters) has been developed based on geometrical acoustics. Using this tool, we have designed and implemented various focused and steered beams for the immersion inspection of copper materials (Chap. 9). It should be noted that the tool can also be used to design focused and steered beams in homogeneous media (e.g., in the contact inspection case).

9 Detection and resolution limits of ultrasonic inspection

9.1 Introduction

Ultrasonic inspection of copper canisters and EB welds in the canisters may be limited by various factors. The detectability of the defects in the welds is limited by grain noise. The regions close to the outer walls of the canisters are often difficult or even impossible to reach by means of normal incident beams due to the geometry of the canisters. Defect sizing is often limited by the lateral resolution determined by the aperture size. The aim of this task is to investigate the detection and resolution limits using the capacity of beam forming available on the ALLIN array system. The tool presented in Chap. 8 was used for designing the beams. The investigation includes the following four experiments.

(i) The first experiment was intended to design and then evaluate the focusing laws for producing the best focused beams for the immersion inspection of EB welds. These focusing laws were implemented on the ALLIN system, and the focused beams were evaluated based on the images of copper block CU2 containing a set of side-drilled holes at different depths. This beam evaluation enabled selection of an optimal focusing law for generating focused beams best suitable for EB weld inspections.

(ii) The second experiment was aimed at evaluating the detection limit. Various artificial defects, such as side-drilled, flat-bottom and round-bottom holes, that were located in the weld zone of a canister segment were inspected using the beams designed in (i). From the analysis of images of the defects, the detection limit was assessed.

(iii) The third experiment was performed for the evaluation of detection limit for defects located close to the outer walls of a copper block and a copper canister. The zones close to the outer wall of a copper block were inspected using focused beams that were steered by various angles. The block contained five sets of flat-bottom holes, each set with a hole diameter different from the others. But this experiment and the results are not presented here. See report [11] for the details.

(iv) The forth experiment was performed in order to investigate the detection limit in a more realistic situation. Two canister segments have been inspected which had side-drilled holes with various depths and sizes located in the EB weld zones. The beams used were focused and steered through various angles.

9.2 Design of optimal focused beams

For either of the 16- and the 32-element apertures, focusing laws were designed to focus beams at 20, 32, 40, 52, 60, 72, 80 mm in the copper block, respectively. In sequel, the focusing laws for the 16-element aperture are denoted by Foc20E16, Foc32E16, …, Foc80E16, *etc.*, and those for the 32-element aperture by Foc20E32, Foc32E32, …, Foc80E32, *etc*. For the 16-element aperture, one more focusing law was used, which focused beam at 12 mm in the block. The corresponding focusing law for the 32-element aperture could not be realized in the ALLIN system because some delay times in the focusing law were larger than 975 ns, which is the upper limit of delay time available for the reception. This shows one of the limitations of the ALLIN system to designing focused and steered beams. All these focused beams created by the 16- and 32-element apertures have been evaluated based on the imaging of copper block CU2 [11]. Only two representative results are presented that were obtained using the focusing laws, Foc60E16 and Foc60E32, for focusing at 60 mm in the block.

Fig. 9.1 shows the B-scans (of the copper block CU2) obtained using the focused beams from (a) the 16-element and (b) the 32-element aperture, respectively. Each of the B-scans is displayed in the depth range of 9 – 73 mm in the block CU2 (in the z direction) and from 0 to 290 mm in the x direction. In each of the B-scans, we can see 15 holes. Each B-scan image is completed by the projections to the y- and z-axis, respectively, above and on the right hand side. The projections to the y- and z-axis facilitate the analysis of resolutions, lateral and axial, respectively. The –3 dB beam widths (BM, in mm) in the figure were measured based on the projections to the x-axis.

Based on the respective B-scans and projections, we have examined all the focused beams generated by investigated the focusing laws and found that :

(i) The positions of the focal zones moved downwards as the beams were focused deeper in the block, and the deeper the focal point the larger the focal zones, which agrees with the theory;

(ii) The projections to the x-axis have shown that in the focal zone the beam widths of shallowly focused beams are narrower and their amplitudes are larger than those of deeper focused beams;

(iii) From the projections to the z-axis it can be seen that the axial resolutions, determined by the duration of pulse excitations, are almost the same in all cases.

Comparing the results from the 16-element aperture with the corresponding ones from the 32-element aperture, we can conclude:

(i) that the larger the aperture, the sharper the focusing and the smaller the focal zone, because of the faster beam convergence to and the faster divergence off the focal point; and

(ii) that the larger aperture give larger echo signal for a given gain.

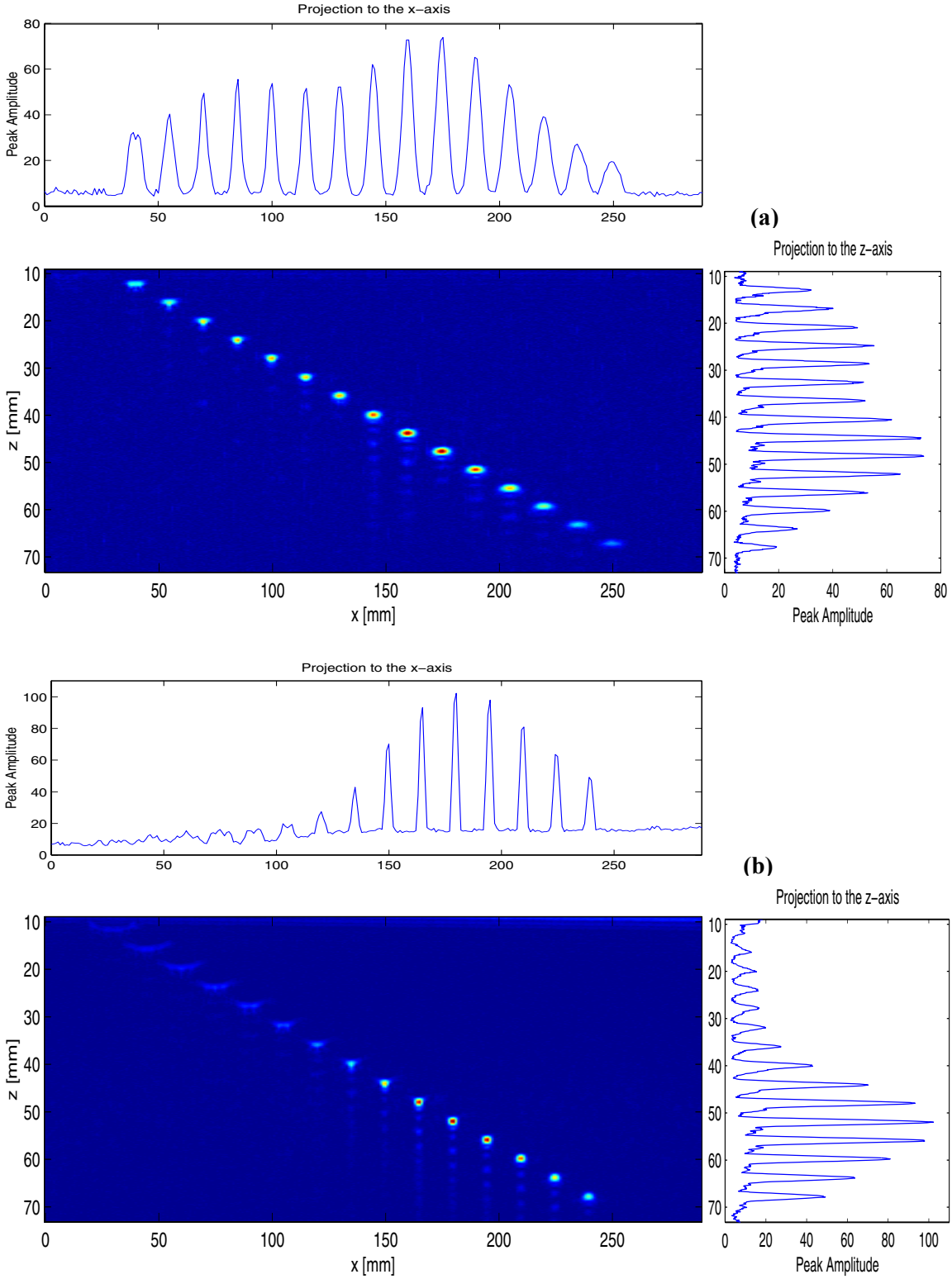

Fig. 9.1. The focused beams by the 16-element (a) and 32-element (b) apertures, respectively, into copper immersed in water with the focal point being located at 60 mm and with a water path of 28 mm.

The results also show that for a given aperture the focusing in the near field region gives a sharper focal zone than the one in the far field region, and generates a focal zone at the position closer to what is expected from the focusing law. The conclusions made and the results obtained are all in agreement with existing theories.

Knowledge about the behavior of beams is very helpful for us to select the beams best suited for the specified inspection. For example, the imaging of the all the holes using the 16-element aperture (Fig. 9.1(a)) shows more uniform than that using the 32-element aperture (Fig. 9.1(b)), (the widths of the holes in Fig. 9.1(a) do not differ so much those in Fig. 9.1(b)). Therefore, when a uniform imaging (especially in B-mode) is needed, the smaller aperture is preferred. When sizing defects or acquiring a C-scan of an EB weld layer, sharp focusing in the region of interest is desired, and, in this situation, the larger aperture (the 32-element aperture) should be a better choice.

9.3 Inspection of EB welds in CAN 1 with focused beams

Since the EB weld zone is a layer located at a depth of approx. 60 mm in the canister, a suitable choice is a beam that has a good resolution in the weld zone and a focal zone covering the weld layer in the *z* direction. Thus, we chose the beam produced by the 32-element aperture with focusing law Foc60E32. For the sake of comparison, we also used the focused beam produced by the 16-element aperture with focusing law Foc60E16. The copper canister block CAN 1 was inspected. In the EB weld in CAN 1, 13 holes were drilled: three side drilled holes (SDH, #1 - #3, and #10 - #13), three flat-bottom holes (FBH, #4 - #6), and three round bottom holes (RBH, #7 - #9). Here the six bottom-drilled holes are of most interest because the beam resolution is under investigation. The electronic scanning and mechanical scanning were performed along the *x* and *y* directions, respectively.

Figs. 9.2 and 9.3 show two C-scans from the focused beams, Foc60E16 and Foc60E32, respectively. They all cover the six bottom-drilled holes (holes #4 - #9). The three FBHs' are clearly seen, and two RBHs' (#7 and #9) are possible to recognize, but RBH #8 is difficult to see. Comparing these two figures, we can say that the beam resolutions in the *y* direction in both cases are almost the same but those in the *x* direction differ quite a lot. That is, in the *x* direction, the resolution of the beam radiated by the 32-element aperture is much better than that by the 16-element aperture. The -3 dB widths of the peaks were measured which corresponded to the echoes from FBHs #4, #5 and #6. They are 7.03, 6.24 and 6.90 mm, respectively, in the case of 16-element aperture with Foc60E16, and 3.40, 3.48 and 4.09 mm, respectively, in the case of 32-element aperture with Foc60E32. The measured data show that the resolution in the latter case is two times higher than the one in the former case. Therefore, for defect sizing in the weld zone, a larger aperture yields better performance.

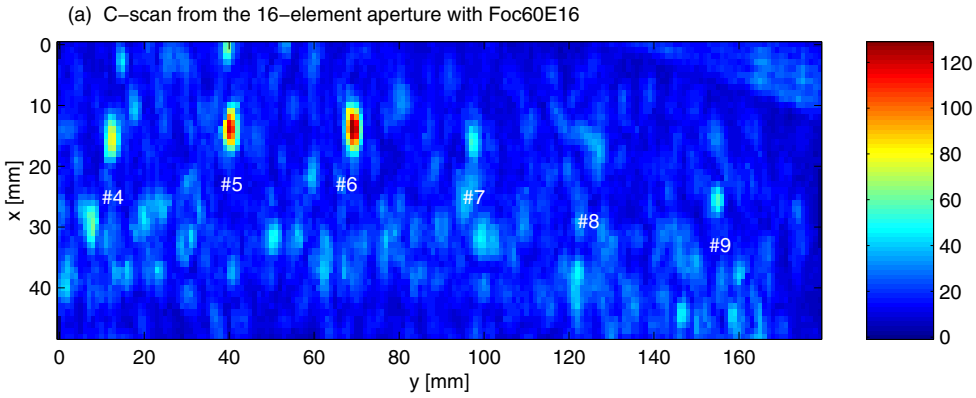

Fig. 9.2. C-scan of the weld zone obtained from the 16-element aperture with Foc60E16.

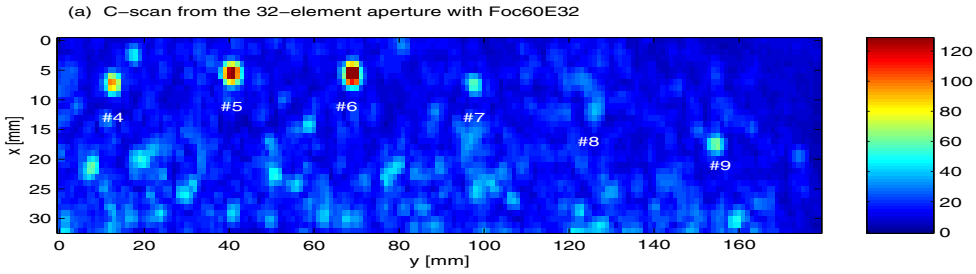

Fig. 9.3. C-scan of the weld zone obtained from the 32-element aperture with Foc60E32.

9.4 Detection of defects close to the outer wall of copper blocks and canisters with steered beams

To look into the detectability of defects close to the outer wall of copper blocks and canisters, we used steered beams to inspect a copper block (CU3) and two copper canisters (CAN 1 and Weld W123) [11]. Here we only present the inspection of CAN 1, which is representative of the overall results.

Since the copper canister CAN1 has a cut corner on the top surface, the weld zone close to the outer wall of a copper canister could not be inspected using a normal incident beam (see Fig. 9.4(a)). Due to the presence of strong structure noise scattered from the weld, the defects in the weld are difficult to distinguish from the structure noise. Therefore, the use of focused, angle beams became necessary for the inspection of the weld zone close to the outer wall. To investigate the detection limits in the weld zone close the outer wall, we used canister CAN1 with four side-drilled holes, two with diameter 2-mm diameter (SDH #10 and #11) and two with 1-mm diameter (SDH #12 and #13). SDHs #10 and #12 are 4 mm deep, and SDHs #11 and #13 are 2 mm deep.

In THE measurements, the ALLIN array performed electronic scanning along the *x* direction and mechanical scanning along the *y* direction. The water path was 28 mm long. the beams used were

steered through 0, 3, 5, 8, 10 and 12 degrees, respectively. All the beams used were focused and the focal points were located at a 60-mm depth in the canister, that is, the depth of the EB weld zone.

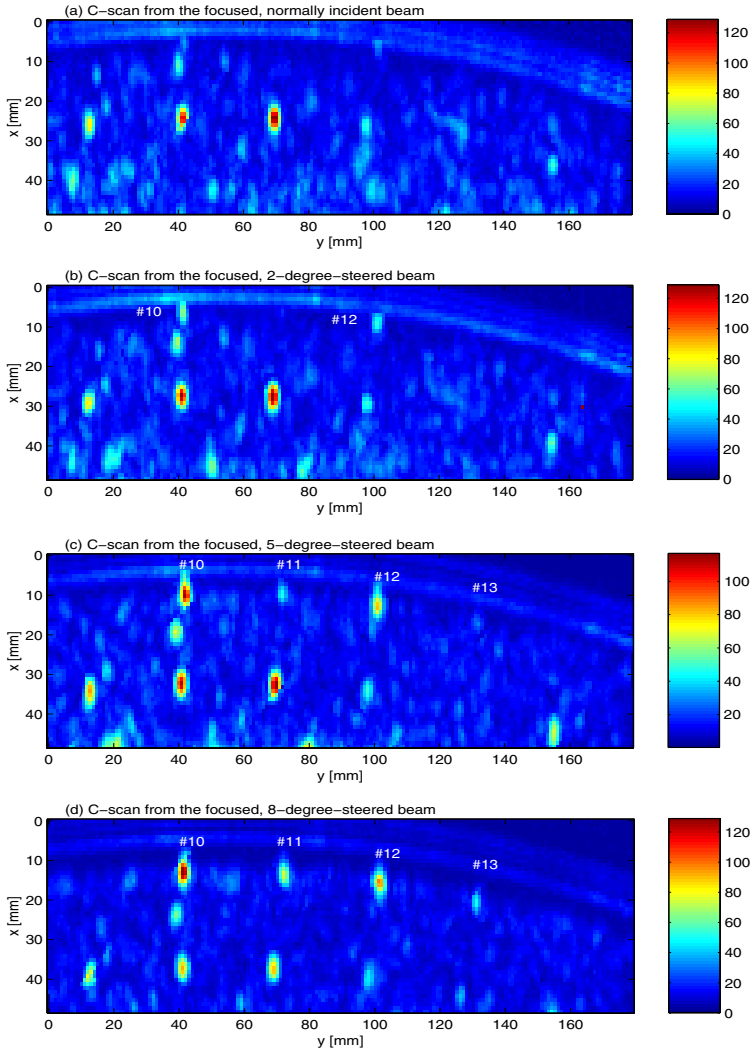

Fig. 9.4. C-scan imaging of the weld in copper canister CAN1 by using focused beams steered by (a) 0 degree, (b) 3 degrees, (c) 5 degrees, and (d) 8 degrees, respectively.

The C-scans obtained using different angle beams are shown in Fig. 9.4. In the case of normal incident beam (Fig. 9.4(a)), the holes (SDHs #10 - #13) of interest are not visible at all; for the beam steered through 2 degrees, SDHs # 10 and #12 can be seen, but SDHs # 11 and #13 still do not appear; for the beam angle of 5 degrees, SDH # 11 comes out, but SDH #13 is still not distinguishable. When the beam was steered through 8 degrees, SDH #13 appears. From these experiments, we see that the use of angle beams is an effective solution to the inspection of the weld zone close to the outer wall of canisters with cut corners.

9.5 Conclusions

Detection and resolution limits have been investigated based on a series of experiments. The results of the experiments coincide with existing theories.

First, the beamforming tool developed and presented in Chap. 8 has been applied to design (electronically) focused beams for the ALLIN array system used in the immersion inspection of copper canisters. The beams focused at different depths have been tested on a copper test block CU 2 with a set of side-drilled holes at different depths. The results have shown that the focusing in the near field region gives a sharper focal zone than the one in the far field region, and generates a focal zone at the position closer to what is expected from the focusing law. Also from the results, it follows that:

- the larger the aperture, the sharper the focusing and the smaller the focal zone, and
- the larger focal zone yields more uniform imaging.

This study has provided us with good knowledge about the behavior and performance of the focused beams so that we could select the best suited beams for the specified inspections.

Secondly, the EB weld in the copper canister CAN 1 with artificial defects (like flat- and round-bottom holes) located in the weld zone has been inspected using the focused beams from the 16- and 32- element apertures. The results showed that the larger aperture yields better performance of defect sizing in welds due to the better lateral resolution.

Thirdly, the beamforming tool has been applied to the design of focused and steered beams used for the inspection of zones close to the outer walls of materials. The welds of the two copper canister segments with shallow side-drilled holes have been examined using the focused, steered beams. These experiments have demonstrated that the use of focused, steered beams is a very effective solution to the inspection task in the zone close to the outer walls of copper canisters.

10 Transducer characterization

10.1 Introduction

This task was motivated by the fact that the measured pulse-echo fields were poorly matched with the calculated results obtained using the nominal geometrical parameters (GPs) and the theory that was based on the extended angular spectrum approach (ASA) (see Fig. 10.1). This mismatch is due to the deviation of the transducer practical behavior from the piston assumption imposed in the theory. This deviation has led to the definition and use of effective GPs for the transducers.

The aim of this task was to characterize both the ALLIN array as well as the two spherically focused transducers in the two-element annular array. The effective geometrical parameters determined in this task for the array and the transducers were expected to improve accuracy of the measurements predictions obtained from the piston model.

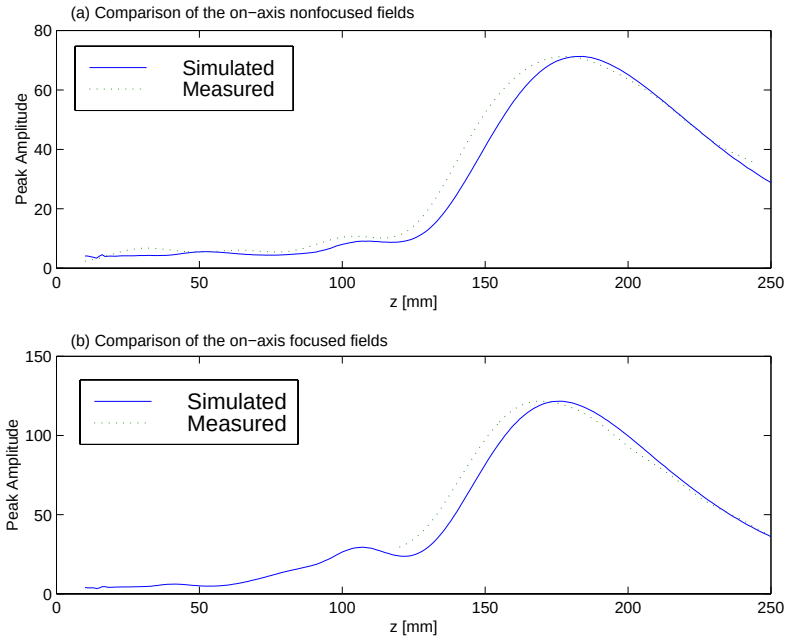

Fig. 10.1. Simulated nonfocused and focused fields (solid) in terms of peak amplitude based the nominal parameters of the ALLIN array and comparison with measured ones (dotted).

The characterization method for the ALLIN array was first proposed and established based on the extended ASA and the temporal Fourier transform. This method is a kind of trial-and-error method; thus, it is not very accurate. Later when the two-element annular array was employed to estimate the attenuation in copper canisters, a more efficient, and simpler method for transducer characterization was developed. It is based on the spatial impulse response method, and relatively easy to implement. It requires a less cumbersome procedure than the existing methods developed for continuous waves.

10.2 Characterization of the ALLIN array

The ALLIN array is a 64-element linear array with a cylindrically concave surface. We have mostly used an aperture consisting of 16 elements in our experiments. The geometry of such an aperture with a cylindrically concave surface is defined by three geometrical parameters: aperture width, aperture length, and focal length (see Fig. 2.3). This indicates that three effective GPs need to be determined for the aperture characterization.

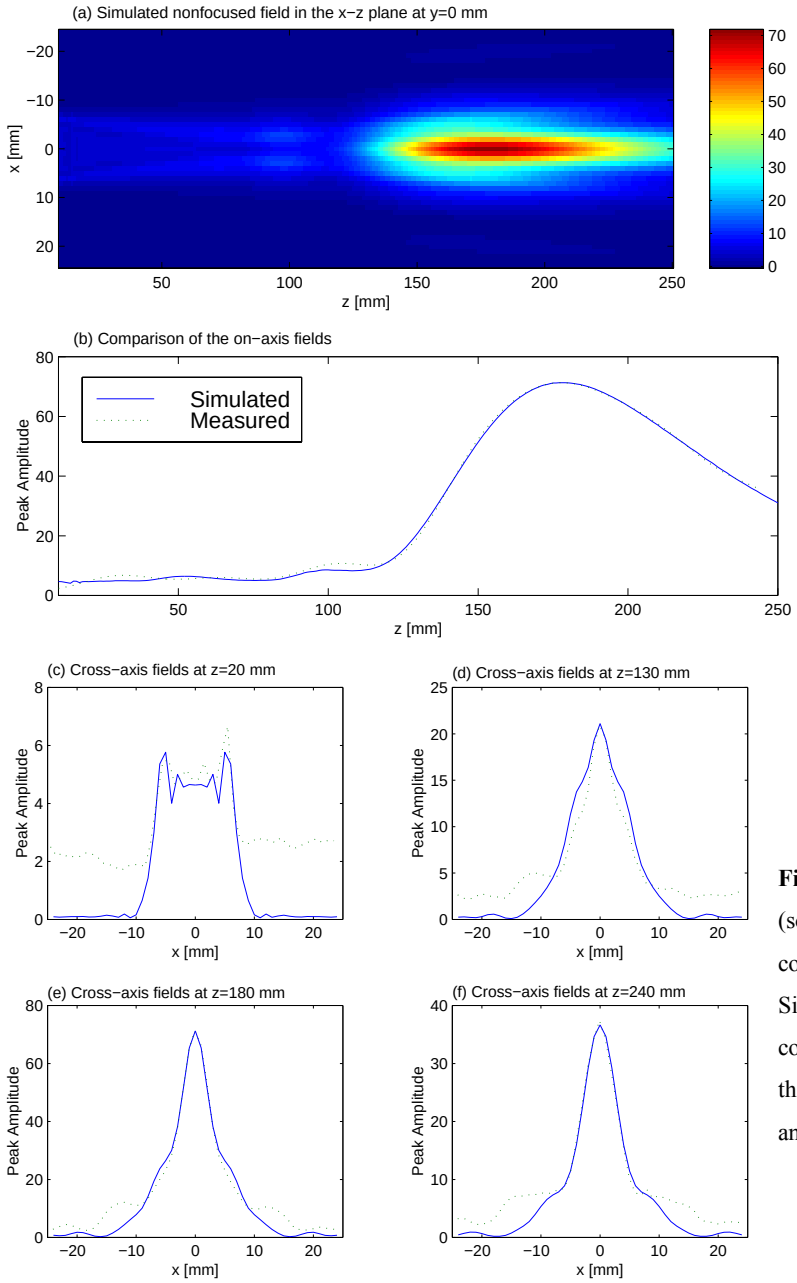

Fig. 10.2. Simulated nonfocused fields (solid) in terms of peak amplitude and comparison with measured ones (dotted). (a) Simulated field in the *x*-*z* plane at $y = 0$, (b) comparison of the on-axis fields, and (c) - (f) the profiles of the fields at $z = 20$, 130, 180, and 240 mm, respectively.

The GPs of a transducer given in the manufacturer's specification are usually nominal. When using the nominal parameters in the theory based on the extended ASA and the temporal Fourier transform, we found that the pulse-echo fields calculated with the theory could not match the measured ones (see Fig. 10.1). Therefore, we made an effort to determine the effective parameters for the ALLIN array. The method characterizing the ALLIN array is based on the extended ASA (that has been presented in Sect. 2.2.1) and the temporal Fourier transform. The effective GPs found were the effective radius of curvature, R=187 mm, and the effective length, 2b=31 mm. Using the effective parameters for the array, we calculated the electronically nonfocused and focused fields in the x-z plane in terms of peak amplitude.

Here we present the calculated results for the electronically nonfocused fields, which are plotted with solid curves in Fig. 10.2 in comparison with the measured results (dotted curves). In the figure, (a) shows the simulated fields in the x-z plane in color scale levels, (b) shows the field on the axis, and (c)-(f) show the cross-axis fields at z = 20, 130, 180 and 240 mm, respectively.
The comparison shows a very good agreement between the simulated and measured fields.

10.3 Characterization of spherically focused transducers

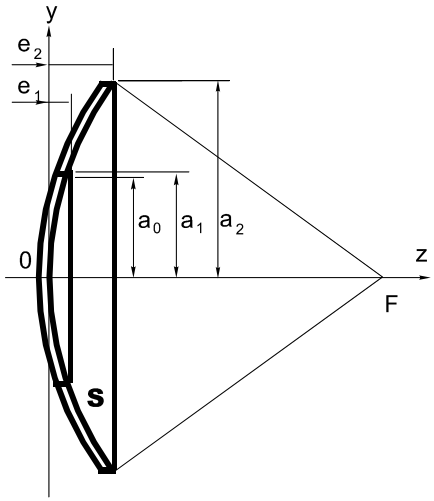

Fig. 10.3. Geometry of the spherically focused transducer with two concentric elements.

The transducer to be characterized is a two-element annular array shown in Fig. 10.3 (mentioned in Chap. 9.3.1). It consists of two concentric elements with radius of curvature of 210 mm (that is the focal length, denoted by F in the figure). The inner element is spherically circular with a 10-mm radius (denoted by a_0), and the outer is spherically annular with a 10-mm inner radius (denoted by a_1, neglecting the gap between the elements) and a 19-mm outer radius (denoted by a_2). The outer and inner elements have the center frequencies of 2.3 and 4.8 MHz, respectively. For a spherical circular transducer, two parameters: radius a_0 and focal length F are to be found. For a spherical annular transducer, three parameters, inner and outer radii, a_1 and a_2, and focal length F, are to be determined.

10.3.1 Characterization method and its theory

The method used for characterizing a spherical circular transducer is established based on the spatial impulse response method (SIRM). In the SIRM a pressure field $p(\mathbf{r}, t)$ at any point $\mathbf{r}$ is calculated by convolving the normal velocity $v_n(t)$ on a transducer surface with the derivative of the transducer's spatial impulse response (SIR) $h(\mathbf{r}, t)$,

$$p(\mathbf{r},t) = \rho_0 v_n(t) * \frac{\partial h(\mathbf{r},t)}{\partial t} = v_n(t) * h_p(\mathbf{r},t), \tag{10.1}$$

where $*$ represents the temporal convolution and ρ_0 is the density of the medium,

$$h_p(\mathbf{r},t) = \rho_0 \frac{\partial h(\mathbf{r},t)}{\partial t}, \tag{10.2}$$

which is usually referred to as the pressure spatial impulse response.

In pulse-echo mode (echo from a point scatterer) the output of a transducer can be calculated by

$$V(t) = V_0 v_n(t) * h_p(\mathbf{r},t) * h_p(\mathbf{r},t) = V_0 v_n(t) * h_{pe}(\mathbf{r},t) \tag{10.3}$$

where V_0 is a proportional constant, and

$$h_{pe}(\mathbf{r},t) = h_p(\mathbf{r},t) * h_p(\mathbf{r},t) \tag{10.4}$$

is called echo pressure SIR.

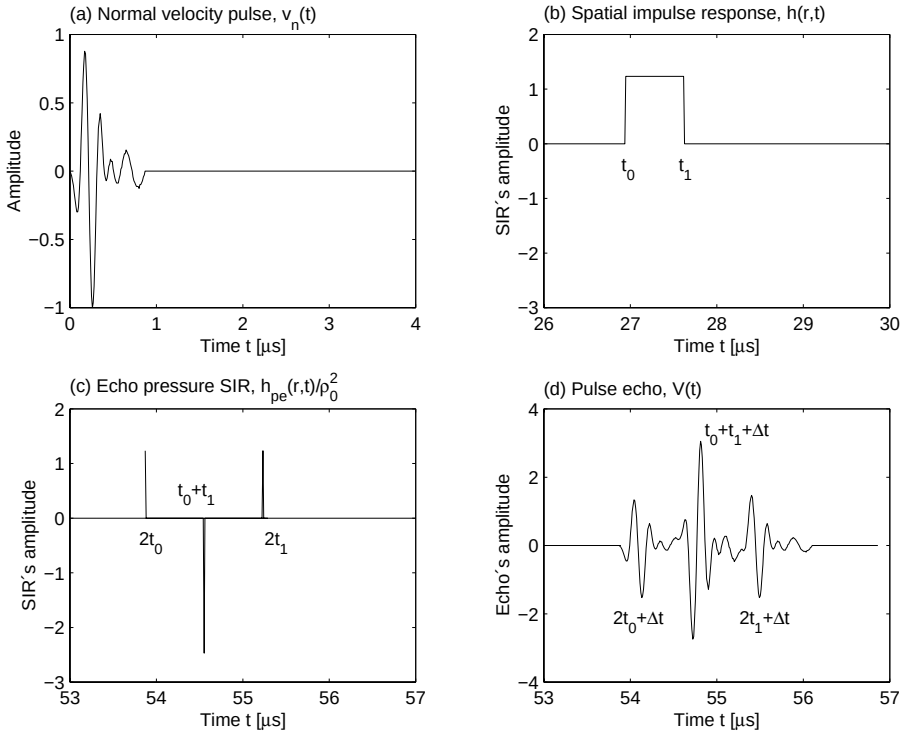

Fig. 10.4. (a) The normal velocity pulse on the spherically circular transducer, (b) the spatial impulse response (SIR) on the axis at z=40 mm, (c) the echo pressure SIR, and (d) the output of the transducer, the pulse-echo from the point scatterer.

A. Characterization of a spherically circular transducer

The characterization method for a spherically circular transducer is established as follows. It is assumed that we have a normal velocity pulse $v_n(t)$ obtained from a measurement (Fig. 10.4(a)). The SIR $h(\mathbf{r}, t)$ can be calculated analytically (see [22]). At the position, y=0 and z=40 mm, and with the nominal radius (10 mm) and focal length (210 mm), $h(\mathbf{r}, t)$ is a rectangle shown in Fig. 10.4(b). The starting and ending instants of the rectangle, t_0 and t_1, are important, which are related to the GPs of the transducer in the following manner

$$t_0 = z/c\,, \tag{10.5a}$$

$$t_1 = \sqrt{a^2 + (z-e)^2}\,/c\,, \tag{10.5b}$$

where

$$e = F - \sqrt{F^2 - a^2}\,. \tag{10.6}$$

At t_0 and t_1 the derivatives of $h(\mathbf{r}, t)$ are two pulses (two $\delta(t)$ functions) with the same amplitude but with opposite signs. The first $\delta(t)$ is positive and results in the direct wave, and the second is negative (the inverted replica of the first) and results in the edge wave. The echo pressure SIR $h_{pe}(\mathbf{r},t)$ obtained by convolution in Eq. (10.4), and displayed in Fig. 10.4(c), has three spikes. The spikes take the form of Dirac pulses at time instants $2t_0$, t_0+t_1 and $2t_1$, separated by time difference $(t_1 - t_0)$. The transducer output shown in Fig. 10.4(d) (a pulse echo from the point scatterer) is proportional to the result of convolution of the normal velocity pulse $v_n(t)$ with the echo pressure SIR $h_{pe}(\mathbf{r},t)$ (c.f., Eq. (10.3)). The three pulses in the received signal $V(t)$ start at time instants $2t_0$, t_0+t_1 and $2t_1$, respectively. Since the time separations of the adjacent pulses are smaller the pulse duration of the normal velocity $v_n(t)$, the three pulses partly overlap. Therefore, the two time instants, t_0+t_1 and $2t_1$ cannot be distinguished from $V(t)$. This can be overcome by measuring three other time instants (e.g., at the second negative peaks of the first and third pulses and the second positive peak of the second pulse) that all have such a time delay Δt that the first and second pulses do not overlap with the second and third one, respectively, at the delayed instants ($t_0+t_1+\Delta t$ and $2t_1+\Delta t$). Thus, the time differences of the three successively measured instants ($2t_0+\Delta t$, $t_0+t_1+\Delta t$ and $2t_1+\Delta t$) are the same, that is $t_1 - t_0 = \Delta t_{10}$.

The method for characterizing spherically circular transducers is first to measure Δt_{10} and then to find the transducer parameters from Δt_{10} using the following relation

$$\Delta t_{10} = t_1 - t_0 = \left(\sqrt{a^2 + (z-e)^2} - z \right) \Big/ c \,. \tag{10.7}$$

Since two parameters, a and F, are to be determined, we need two measurements at two distances. Assuming that the two time differences Δt_{10}^{I} and Δt_{10}^{II} are obtained from two measurements at z_I and z_{II}, then we can determine the effective radius and focal length,

$$a_{eff} = \sqrt{\left(c\Delta t_{10}^{I} + z_I\right)^2 - (z_I - e)^2} \,, \tag{10.8}$$

$$F_{eff} = \left(a_{eff}^2 + e^2\right) \Big/ 2e \,, \tag{10.9}$$

where

$$e = \frac{\left(c\Delta t_{10}^{I}\right)^2 - \left(c\Delta t_{10}^{II}\right)^2 + 2c\left(\Delta t_{10}^{I} z_I - \Delta t_{10}^{II} z_{II}\right)}{2\left(z_{II} - z_I\right)} \,. \tag{10.10}$$

B. Characterization of a spherically annular transducer

To characterize a spherically annular transducer, we have to determine three geometrical parameters, inner and outer radii, and focal length. Using a similar method, we formulate a similar procedure for the SIRM to calculate a pulse echo from a point scatterer for the annular transducer, shown in Fig. 10.3. We obtain a normal velocity pulse from measurements (Fig. 10.5(a)).

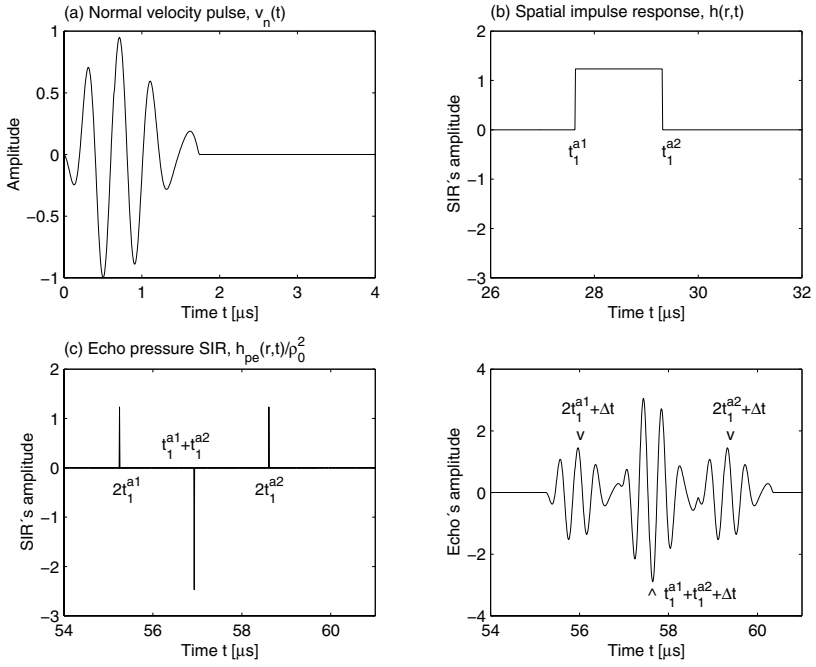

Fig. 10.5. (a) The normal velocity pulse on the spherically annular transducer, (b) the spatial impulse response (SIR) on the axis at z=40 mm, (c) the echo pressure SIR, and (d) the output of the transducer, the pulse-echo from the point scatterer.

For the annular transducer there is no direct wave present but there are two edge waves from the edges of the inner and outer circles, respectively. The SIR is shown in Fig. 10.5(b). The echo pressure

SIR in Fig. 10.5(c) has three spikes at different time instants determined by $2t_1^{a1}$, $t_1^{a1}+t_1^{a2}$ and $2t_1^{a2}$, respectively. Here t_1^{a1} and t_1^{a2} are expressed by

$$t_1^{a1}=\sqrt{a_1^2+(z-e_1)^2}\,\big/c, \tag{10.11a}$$

$$t_1^{a2}=\sqrt{a_2^2+(z-e_2)^2}\,\big/c, \tag{10.11b}$$

where

$$e_1=F-\sqrt{F^2-a_1^2}\,, \tag{10.12a}$$

$$e_2=F-\sqrt{F^2-a_2^2}\,. \tag{10.12b}$$

If using a similar approach as for the spherically circular transducer, we have

$$\Delta t_{11}=t_1^{a2}-t_1^{a1}=\left[\sqrt{a_2^2+(z-e_2)^2}-\sqrt{a_1^2+(z-e_1)^2}\right]\Big/c\,. \tag{10.13}$$

From three on-axis measurements at three different distances, z_I, z_{II} and z_{III}, we can find the effective inner and outer radii, and the focal length. However, it is tedious and difficult to solve the set of three equations Eq. (10.13). Therefore, we circumvent this difficulty by using an alternative means, that is, using the time differences between the corresponding time instants obtained from different measurements, see [22,26] for details.

The methods developed for characterizing both the spherically circular and annular transducers based on the SIRM are referred to as *spatial impulse response characterization methods* (SIRCM).

10.3.2 Measurements and transducer characterization

The measurements needed for the transducer characterization were conducted in water in pulse-echo mode. A small drill (0.3-mm in diameter) with a flat end directed towards the transducer was used as the approximation of a rigid point scatterer. Care must be taken when measuring some parameters, like sound velocity and distances of transducer movements. Since sound velocity in water varies with temperature, it had to be measured each time when acoustic field measurements were conducted.

Another important thing is to find the transducer axis precisely. This can be done by scanning the point scatterer across the transducer axis (actually the transducer is scanned and the scatterer is fixed) so that a cross-sectional image of the field is obtained. For example, Fig. 10.6 shows two cross-sectional images of fields from the small scatterer located at z = 35 and 40 mm, respectively. From each of these images we can easily locate the on-axis signal.

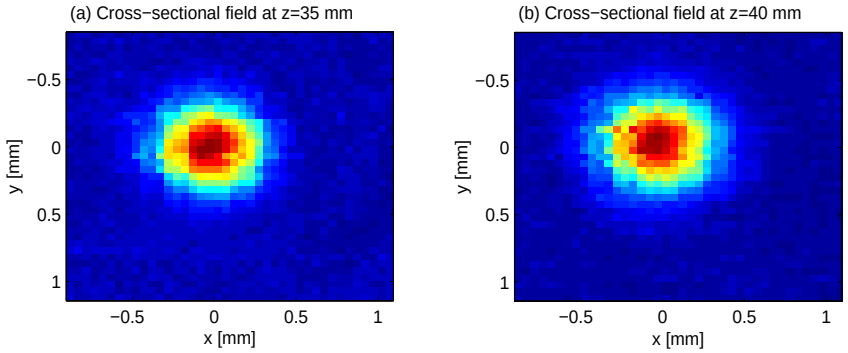

Fig. 10.6. Cross-sectional images of pulse-echo field for the spherical annular transducer from the small scatterer located at (a) z=35 mm and (b) z=40 mm.

Two measurements were made for a spherically circular transducer at two different distances, the pulse-echo signals identified as closest to the transducer axis are shown in Fig. 10.7(a) and (b). Inserting the measured values into Eqs. (10.8)-(10.10) resulted in a_{eff} = 9.86 mm and F_{eff} =223.5 mm (the nominal parameters: a= 10 mm and F = 210 mm).

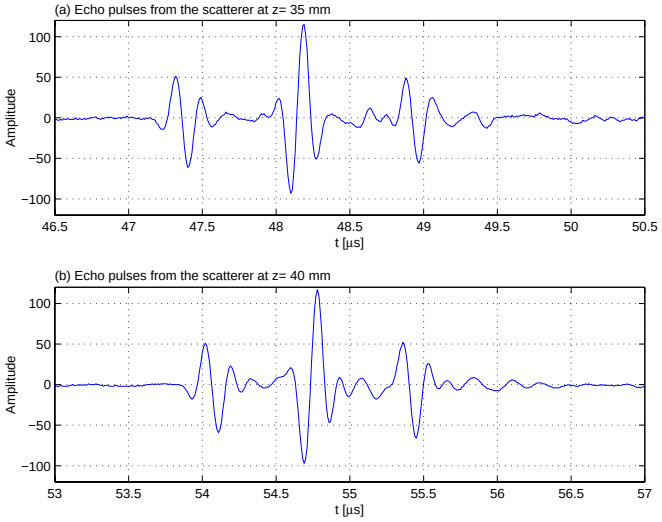

Fig. 10.7. Echo pulses of the spherical circular transducer that come from the small scatterer located at (a) z=35 mm and (b) z=40 mm.

In a similar way, we characterized a spherically annular transducer that has three geometrical parameters: inner and outer radii and focal length, had to be determined.

We chose three measurements made at three different distances, and the pulse-echo signals closest to the transducer axis were selected. Putting the measured values in Eqs. (10.16) – (10.18) yielded: a_{1eff} =10.7 mm, a_{2eff} =18.3 mm, and F_{eff} =232 mm (the nominal values were: a= 10mm, a_2= 19 mm and F= 210mm). The obtained effective GPs were put into the SIRM-based model, and then the respective pulse-echo fields were calculated and compared with the measured ones. The comparison has demonstrated that using the effective GPs in the SIRM-based model provides a good prediction. This is presented in detail in the 2000 report [22].

10.4 Conclusions

Two methods for transducer characterization, that is, for determining the effective GPs of transducers, have been developed. The first method, proposed for characterizing the ALLIN array, was based on the extended angular spectrum approach (ASA) and the temporal Fourier transform. The effective GPs in this method are determined in a trial-and-error way, which limits its accuracy.

The second method used for determining effective GPs of spherically focused transducers is based on the time-domain approach (SIRM). The effective GPs, radius and focal lengths, of a spherically focused transducer were found using simple algebraic calculations and measurements of the time differences between the direct and edge waves in the pulse-echo signals from a small scatterer. The experimental setup for measuring the pulse-echo signals is simple. Thus, the proposed method is relatively easy to implement and requires simpler measurement setup than the existing methods that were developed using frequency domain approach. The proposed method is best suited for broadband transducers with short pulse excitations. For narrowband transducers, the method may be applied using some type of deconvolution. The method also applies to transducers of other shapes, e.g., planar circle, and planar or curved rectangle provided that these transducers have on-axis SIRs in analytical form.

11 Conclusions and future work

Research concerned with the inspection of copper canisters for spent nuclear fuel by means of ultrasound carried out at Signals and systems, Uppsala University in years 1994-2000 has been summarized in this report.

Main goal of the project was demonstrating the feasibly of ultrasonic array technique for the inspection of canister welds and getting know-how needed for the successful application of this method in the future SKB´s canister factory.

The research work includes both the theoretical tasks, such as modeling of wave propagation, and the experimental tasks, like characterization and calibration of the ultrasonic system ALLIN. Important issues such as, material and grain noise characterization, processing ultrasonic signals, ultrasonic imaging, have also been addressed. The work included both developing new methods (for example, field modeling and transducer characterization) and applying known techniques (for instance, estimation of attenuation and velocity).

Looking from the time perspective the whole project has been successful, which means that the main goal or at least its first part has been achieved. The array technique has been successfully used at SKB's Canister Lab and it has provided the users with pertinent information that was especially valuable during start up phase of the electron beam welding equipment. However, the second part of the goal, gathering the know-how, is unlimited by its nature and we intend to continue our efforts in this direction in the future. This means that we aim to develop methods that will refine the existing array technique by improving the detectability of defects and increasing the reliability of detection.

This can be achieved through the improving ultrasonic imaging by using such techniques as, harmonic imaging, synthetic aperture focusing technique (SAFT) and deconvolution. Harmonic imaging has been already preliminarily investigated, the results were encouraging and this research will be continued. A preliminary study of SAFT has yielded positive results and we will continue work focused on combining physical and synthetical focusing. An extensive study of techniques for enhancing the temporal resolution has been carried out in our group [cf., 28] and its results will also be applied in this project.

12 References

[1] P. Wu, R. Kazys and T. Stepinski, "Analysis of the numerically implemented angular spectrum approach based on the evaluation of two-dimensional acoustic fields--Part I: Errors due to the discrete Fourier transform and discretization," *J. Acoust. Soc. Am.* **99:** 1339-1348 (1996).

[2] P. Wu, R. Kazys and T. Stepinski, "Analysis of the numerically implemented angular spectrum approach based on the evaluation of two-dimensional acoustic fields--Part II: Characteristics as a function of angular range," *J. Acoust. Soc. Am*. **99:** 1349-1359 (1996).

[3] P. Wu, R. Kazys and T. Stepinski, "Optimal selection of parameters for the angular spectrum approach to numerically evaluate acoustic fields," *J. Acoust. Soc. Am.,* **101**, pp. 125-134, (1997).

[4] P. Wu, R. Kazys and T. Stepinski, "Calculation of transient fields in immersed solids radiated by linear focusing arrays," in 1995 *IEEE Ultrason. Symp. Proc.*, pp. 993-997, 1995.

[5] T. Stepinski and P. Wu, "Inspection of copper lined canisters for nuclear waste fuel using ultrasonic arrays," *Proc of the 14th International Conference on NDE in the Nuclear and Pressure Vessel Industries*, pp. 519-524, Stockholm, Sept. 24-26, 1996.

[6] T. Stepinski, and P. Wu, *Ultrasonic Inspection of Nuclear Fuel Copper Canisters*, SKB Projektrapport 97-01, December 1996.

[7] T. Stepinski, and P. Wu, *Inspection of Copper Canisters for Spent Nuclear Fuel by Means of Ultrasonic Array System*, SKB Projektrapport 97-06, Augusti 1997.

[8] P. Wu, and T. Stepinski, "Elastic fields in immersed isotropic solids from phased array: the time harmonic case," *Res. Nondestr. Evla.* **10**: 185-204, (1998).

[9] P. Wu and T. Stepinski, "Detection of defects in materials characterized by large grain backscattering using K-distribution model," in *First International Conference on NDE in Relation to Structural Integrity for Nuclear and Pressurised Components*, Amsterdam, The Netherlands, Oct. 20-22, 1998.

[10] T. Stepinski, P. Wu, M. Gustafsson and L. Ericsson, "Ultrasonic array technique for the inspection of copper lined canisters for nuclear waste fuel," *Proc. of 7th European Conference on Non-destructive Testing (7th ECNDT)*, Copenhagen, Denmark, 26-29 May, 1998, pp. 1377-1383.

[11] P. Wu, and T. Stepinski, *Inspection of Copper Canisters for Spent Nuclear Fuel by Means of Ultrasonic Array System - Modelling, Defect Detection and Grain Noise Estimation*, SKB Technical Report TR-99-12, July 1998.

[12] T. Stepinski and P. Wu, "Evaluation of ultrasonic attenuation and estimation of ultrasonic grain noise in copper", in *Proc. Int. Symposium on Material Characterization*, Sydney, July, 1999.

[13] P. Wu, and T. Stepinski, "Extension of the angular spectrum approach to curved radiators," *J. Acoust. Soc. Am.* **105**: 2618-2627, (1999).

[14] T. Stepinski and P. Wu, "Ultrasonic technique for imaging welds in copper," *IMTC/99, 16th IEEE Instrumentation and Measurement Technology Conference*, Venice, Italy, May 24-26, 1999, pp. 856-859.

[15] P. Wu and T. Stepinski, “Investigation of Effective Geometrical Parameters for a Pulse-Echo Linear Array with Cylindrical Curved Focusing Surface,” *Joint EAA/Acoustical Society of America Meeting*, Berlin, Germany, March 14-19, 1999.

[16] P. Wu and T. Stepinski, “An Approach to Calculating Spatial Impulse Response of Curved Transducers: Linear Arrays with Cylindrically Curved Surfaces,” *Joint EAA/Acoustical Society of America Meeting*, Berlin, Germany, March 14-19, 1999.

[17] P. Wu, Fredrik Lingvall, and T. Stepinski, *Inspection of Copper Canisters for Spent Nuclear Fuel by Means of Ultrasonic Array System – Electron Beam Evaluation, Modelling, and Materials Characterization*, SKB Technical Report TR-99-43, December 1999.

[18] P. Wu, and T. Stepinski, " Spatial impulse response method for predicting pulse-echo fields from a linear array with cylindrically concave surface," *IEEE Ultrason. Ferroelec. Freq. Contr.*, vol. 46, no. 5, pp. 1283-1297, 1999.

[19] P. Wu, and T. Stepinski, "Quantitative estimation of ultrasonic attenuation in a solid in the immersion case with correction of diffraction effects," *Ultrasonics,* vol. 38, pp. 481-485, 2000.

[20] T. Stepinski, and P. Wu, “Ultrasonic Imaging of Copper Material Using Harmonic Components,” *2nd International Conference on NDE in Relation to Structural Integrity for Nuclear and Pressurized Components*, New Orleans, USA, 24-25 May, 2000.

[21] P. Wu, and T. Stepinski, “Ultrasonic harmonic imaging in nondestructive evaluation: preliminary experimental study,” *2000 IEEE Ultrason Symp.*, San Juan, Puerto Rico, Oct. 22-25, 2000.

[22] P. Wu, Fredrik Lingvall, and T. Stepinski, *Inspection of Copper Canisters for Spent Nuclear Fuel by Means of Ultrasonic Array System – Electron Beam Evaluation, Materials Characterization* and *Modelling,* SKB Technical Report, TR-00-23, 2000.

[23] Tadeusz Stepinski, and Ping Wu, “Ultrasonic Imaging and Evaluation of Electron Beam Welds in Copper Canisters,” 2001 MRS Spring Meeting, April 16-20, 2001, San Francisco, USA.

[24] Tadeusz Stepinski, Tomas Olofsson and Ping Wu, “Enhancing Resolution in Ultrasonic Imaging Using Transducer Harmonic Components,” 5th International Conference on Theoretical and Computational Acoustics, May 21-25, 2001, Beijing, China.

[25] P. Wu, and T. Stepinski, “Angular space algorithm – a novel algorithm for the angular spectrum approach for axisymmetric transducers,” 5th International Conference on Theoretical and Computational Acoustics, May 21-25, 2001, Beijing, China.

[26] P. Wu, and T. Stepinski, “A spatial-impulse-response-based method for determining effective geometrical parameters for spherically focused transducers,” Ultrasonics International 2001, July 2-5, 2001, Delft, the Netherlands.

[27] L. Ericsson, and T. Stepinski, “Algorithms for Suppressing Ultrasonic Backscattering from Material Structure – A Review”, *Ultrasonics International* 2001, July 2-5, 2001, Delft, the Netherlands.

[28] T. Olofsson and T. Stepinski, “Deconvolution of NDE Signals”, invited paper at *IVth International Workshop Advances in Signal Processing for Non Destructive Evaluation of Materials,* Quebec, Canada, August 7-10, 2001